Quantum Transport Properties and Scattering Mechanisms in Transition Metal Dichalcogenides

by

Kraig J. Andrews

Ph.D. Dissertation Prospectus

February 2016

Advisor

ABSTRACT

Intrinsic Channel Properties, Scattering Mechanisms, and Quantum Transport Properties in Transition Metal Dichalcogenides

by

Kraig J. Andrews

February 2016

Advisor: Dr. Zhixain Zhou
Major: Physics
Degree: Doctor of Philosophy

Since 2004, the isolation of graphene by Novoselov *et al.* the study of graphene and subsequent two-dimensional materials have garnered much interest. The discovery of graphene's lack of band gap led to researchers to search for other viable materials for digital applications. In light of this layered materials, especially transition metal dichalcogenides (TMDs), have been studied extensively. These TMDs are hexagonal structures layered with a metal sandwiched between a chalcogenide layer, for example $\mathrm{MoS_2}$ and $\mathrm{WSe_2}$. These materials have interesting band structures with layer dependence and are considerably strong at the atomic level. With these facts in mind, TMDs have become one of the leading candidates for use in digital circuits, however, some critical challenges remain in order realize this goal.

In this study, we propose novel techniques to study the intrinsic properties of these TMDs, particularly $\mathrm{WSe_2}$ and $\mathrm{MoS_2}$. In order to study these properties, we employ an approach to fabricating low-resistance contacts using degenerately p-doped $\mathrm{WSe_2}$. Using this method, as shown in Chuang *et al.*, resistances as low as $0.175\,\mathrm{k\Omega\,\mu m}$. With the low-resistance contacts we study the intrinsic channel properties in p-doped $\mathrm{WSe_2}$ channel devices to understand and find how the doping content of the channel affects the device's performance for applications using hBN enscapsulation. Using this configuration we find field-effect mobilities of $\sim 200\,\mathrm{cm^2V^{-1}s^{-1}}$ and $\sim 650\,\mathrm{cm^2V^{-1}s^{-1}}$ at $T = 300\,\mathrm{K}$ and $T = 5\,\mathrm{K}$, respectively. In addition, we study the intrinsic channel properties by manufacturing Hall bar devices. To this end, we hope to find the device performance limits for applications. By manufacturing high-quality devices we can study the quantum transport properties by measuring the device properties at low temperatures ($\sim 4\,\mathrm{K}$), namely the integer quantum Hall effect and the Shubnikov-de Haas oscillations. This will allow us to determine quantities like the quantum scattering times, effective cyclotron mass, and the geometry of the Fermi surface.

Table of Contents

List of Figures

List of Tables

Chapter 1

Introduction

1.1 Early Semiconductors

The development of microelectronics revolutionized the world in the latter half of the twentieth century. The term semiconductor, in the sense it is known today, first appears in literature in 1911 [1]. Initially, work on the subject was rather pessimistic. However, in the years following Word War II breakthroughs began shed light on the possible applications and the underlying physics involved, such as the ideas of *instrinsic* and *extrinsic* semiconductors [2, 3, 4, 5].

The history of semiconductors and transistors is a well documented subject. The first transistor was constructed at Bell Labs in 1947 using polycrystalline germanium. Shortly thereafter one was developed using silicon. Throughout the following years, these devices were improved on by replacing polycrystalline with single crystals [6]. Then Jack Kilby demonstrated the first integrated circuit (IC) in 1958, for which he would win the Nobel Prize in physics [7, 8]. The scale of ICs grew rapidly in the subsequent years. Initially only a few transistors could fit on a chip (small-scale integration), in stark contrast to modern-day chips that contains billions of transistors [9, 10]. Growth continued at a rapid pace, but eventually it was realized that some limits, material and integration based, existed in silicon and other commonly used materials [11, 12]. In part, these limitations increased the interest in alternative materials. As a result widespread and renewed interest has led to a breadth information and results on a wide range of materials and their applications.

1.2 Graphene as a New Two-dimensional Material

Layered materials have existed for a long time, and have been studied over the last few centuries [13, 14]. In recent decades the scientific study of graphite (3D) has led to new forms of materials, such as carbon nanotubes (1D) and fullerenes (0D) [15, 16, 17]. However, only more recently have scientists began to understand the potential of such layered materials and their potential technological applications. After attempting unsuccessfully to synthesize few-layer graphite during the 1960s, only around 10-50 layers were able to be synthesized, a breakthrough was finally acheived [16]. This most notably began with the synthesis of monolayer graphene [18].

1.2.1 Properties of Graphene

To date, graphene's properties have been the focus of much research, both theoretical and experimental. It has been one of the primary driving forces in study of 'relativistic' condensed matter physics due to its low dimensionality and its band structure that allows electrons to mimic relativistic particles confirming the appearance of several relativistic phonomena [19, 20, 21, 22]. In its most basic sense, graphene is composed of a single layer of carbon atoms arranged in two-dimensional honeycomb lattice (see fig. 1.1(a)) It has a Young's modulus of $100\,\mathrm{GPa}$ (several times more than steel) with a breaking force that is 13% of its Young's modulus [23, 24]. Its stength is due, in part, to its strong in-plane carbon (C) bonds. In addition, graphene can sustain elastic deformations of 20% due to its two-dimensional nature and it has high pliability [16]. These mechanical properties are of interest because graphene lies in the extreme ranges of many metrics considering its size and dimensionality.

Aside from its mechanical properties, graphene's transport properties were another reason why the material was so appealing. Graphene's mobility is several times that of silicon's (electron mobility $\mu \sim 1400\,\mathrm{cm^2V^{-1}s^{-1}}$, hole mobility $\mu \sim 450\,\mathrm{cm^2V^{-1}s^{-1}}$ at room temperature). Experimental results have shown graphene mobility around $15,000\,\mathrm{cm^2V^{-1}s^{-1}}$ with a potential theoretical limit of $200,000\,\mathrm{cm^2V^{-1}s^{-1}}$ [25, 24, 26]. The upper theoretical limit imposed on mobility is due to scattering, however, these high mobilities are achieved mainly because electrons in graphene act very much like photons in their mobility due to their lack of mass. This enables them to travel sub-micron distances without scattering [27]. In reality, there are other limiting factors that need to be considered such as the quality of graphene and scattering with the substrate, for example.

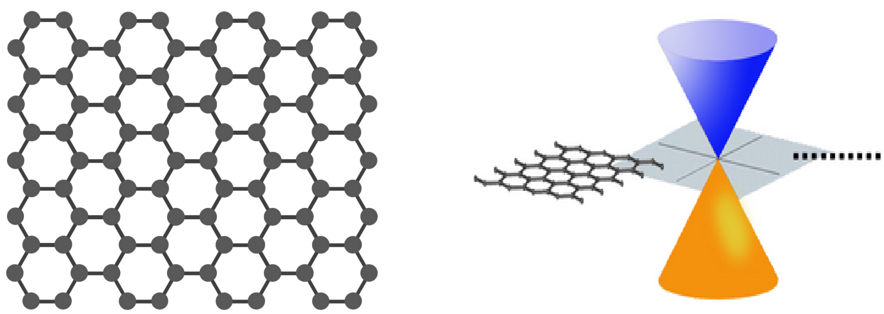

(a) (b)

Figure 1.1: (a) Graphene: a layer of carbon atoms in a honeycomb lattice. (b) One of the most unusual features of graphene is that its conduction and valence bands meet at a point, meaning that in single-layer graphene there is no bandgap (Figures obtained from [28]).

1.2.2 Band Structure of Graphene

Despite its impressive properties, the main drawback of graphene is its lack of bandgap. As this became known, the prospect of using graphene for the fabrication to ICs became unlikely. In graphene the conduction and valence bands touch at a single point as shown in fig. 1.1(b) [29]. Ultimately, the lack of a bandgap means that the current on/off ratio is low and is unappealing for logical circuit applications [30]. However, graphene exhibits some interesting properties as a result of having no bandgap, particularly as it pertains to its optical properties. The material's band structure allows for absorption of light over a large range of the electromagnetic spectrum, ranging from infrared ($< 1.65\,\mathrm{eV}$) to ultraviolet ($> 3.2\,\mathrm{eV}$), offering potential electronic-photonic device applications [31, 32, 33]. Since a direct use in logical circuits is not practical researchers have moved on to look for 'two-dimensional materials beyond graphene.' Several attempts at some derivatives of graphene-like materials have been studied, but for the most part they do not seem promising for use in logical circuits [34, 35]. As of late, research has been concentrated on two-dimensional materials, namely transition methal dichalcogenides, as a candidate in ICs and other potential device applications.

1.3 Two-dimensional Materials: Transition Metal Dichalcogenides

Commonly referred to two-dimensional materials beyond graphene, transition metal dichalcogenides (TMDs) have garnered much interest in recent years. TMDs were studied previously, however, they have gained renewed interest due to their properties [36, 37, 38, 39]. TMDs consist of hexagonal layers of metal (M) atoms in between two layers of chalcogen (X) atoms (see fig. 1.2(b)), such that the stoichiometry of the material is MX_2 [30]. The material is dependent on the type of transition metal, typically one of: molybdenum (Mo), tungsten (W), niobium (Nb), rhenium (Re), nickel (Ni), or vanadium (V), and two chalcogen atoms, typically one of: sulfur (S), selenium (Se), or tellurium (Te) [39, 40]. The most commonly studied variations of TMDs are molybdenum disulfide (MoS_2), tungsten diselenide (WSe_2), and tungsten disulfide (WS_2). These materials are commonly stacked together involving van der Waals interactions between adjacent sheets and covalent bonding within each individual sheet (see fig. 1.2(a)) [30]. TMDs have been

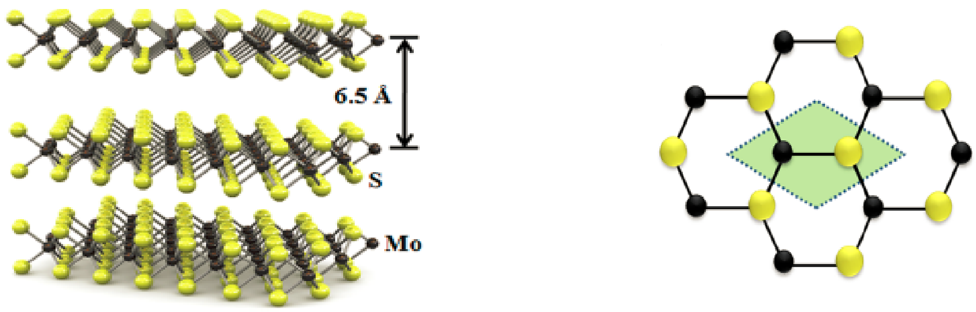

(a) (b)

Figure 1.2: (a) The atomic structure of a layered TMD, depicting MoS_2. Each sheet is composed of three atoms with Mo sandwiched in between two S atoms, S-Mo-S. (b) Top view of a TMD (MoS_2) lattice. (Figures obtained from [41])

found to exhibit a wide variety of interesting properties, including either being a metal or insulator, and displaying the topological insulator effect, superconductivity, and thermoelectricity [42, 43, 44, 45].

2D material	theoretical E_g (eV)	experimental E_g (eV)
graphene	0	0
bilayer graphene	0	0
bulk h-BN	-	5.97 [46]
monolayer h-BN	-	6.07 [47]
few layer (2-5) h-BN	-	5.92 [48]
bulk MoS_2	$1.2^{a,b}$ [49, 50]	$1.0\text{-}1.29^{b}$ [49, 50]
monolayer MoS_2	$\sim 1.90^{a,c}$ [51]	$\sim 1.90^{b}$ [51]
bulk WS_2	$\sim 1.30^{a,b}$ [49, 52]	$\sim 1.35^{c}$ [49, 52]
monolayer WS_2	$\sim 2.10^{a,c}$ [53]	-
bulk WSe_2	-	$\sim 1.20^{b}$ [54]
monolayer WSe_2	-	$\sim 1.7^{c}$ [54]

[a] Theoretical calculations based on first-principles calculations using density functional theory (DFT).
[b] Indirect bandgap semiconductor.
[c] Direct bandgap semiconductor.

Table 1.1: Summary of the bandgaps of typical monolayer, bilayer, and bulk TMDs and h-BN materials. Table adapted from ref. [30].

1.3.1 Band Structures of TMDs

As stated in sec. 1.2.2, one important propert as it pertains to applications for logical circuits is the material's band structure. One of the main reasons TMDs have been so extensively studied lately is due to the fact that, unlike graphene, they do exhibit a bandgap. The bandgaps in some commonly used TMDs is interesting because of the transition from an indirect to a direct bandgap as the layered thickness decreases. Fig. 1.3 illustrates this, for bulk and few-layer MoS_2 there is an indirect band gap while for monolayer MoS_2 there is a direct bandgap. This unusual structure results in some unique optical properties making monolayer TMD promising candidates for optoelectronic devices [55, 56]. Table 1.1 summarizes some TMD bandgap energies that are of considerable interest to the device fabrication process.

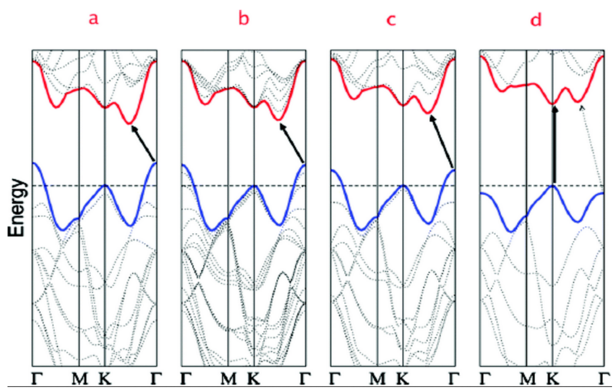

Figure 1.3: Calculated band structures of (a) bulk MoS_2, (b) four-layer MoS_2, (c) bilayer MoS_2, and (d) monolayer MoS_2. Here the solid arrows indicate the lowest energy transitions. (Taken from [57], originally appeared in [58])

1.4 Current Challenges in TMDs and Beyond

There are several challenges facing the advancement of study of TMDs. One of these is the development of low contact resistance devices. The formation of a Schottky barrier (SB) occurs when making electrical contacts [59, 60]. This problem affects many aspects of the growth of TMDs, low contact resistance devices are essential for the study of intrinsic transport properties and performance limits of devices. Two main approaches exist for achieving low-resistance metal-semiconductor contacts. The first of these is lowering the Schottky barrier height (SBH) by choosing metals with proper work functions. Finding metals with the proper work function to minimize the SBH while still maintaining a high conductivity has proven to be difficult [61, 62]. If a proper work function metal were to be found that met the requirements for current TMD performance the effect of lowering the SBH may still be diminished due to Fermi level pinning [63]. Therefore, another method to achieve low-resistance contacts is desirable. The second approach used to achieve low-resistance contacts is to degenerately dope the contact regions. Heavily doping the contact region effectively decreases the SB width [64]. However, this too, has its own challenges associated with it. One possible way to overcome the problems and tune the SB is to use a buffer layer and covering with a material such as hBN or graphene [65, 66, 67, 68]. This second approach has shown promise in reducing the contact resistance and lowering the SB while still maintaining high carrier mobility (see ch. 3).

Aside from the commonly used two-dimensional materials like MoS_2 and WSe_2, black phosphorus (BP) has begun to show promise. Bulk BP has a direct bandgap of $\sim 0.3\,\text{eV}$, which is expected to increase to $\sim 2.0\,\text{eV}$ as the thickness approaches monolayer [69, 70, 71]. In the past few years, few-layer black phosphorus has been shown to have desireable room temperature field-effect mobility ($\sim 1,000\,\text{cm}^2\text{V}^{-1}\text{s}^{-1}$

for ~ 10 layer BP and $\sim 200\,\mathrm{cm^2V^{-1}s^{-1}}$ for 5 nm BP) [72, 73, 74]. BP has shown potential for applications to thin-film electronics and infrared optoelectronics due to its bandgap energy range [75, 74]. In addition, the high mobility measurements have recently allowed for measurements of novel quantum physics, opening the door to further study of intrinsic channel properties of TMDs.

Chapter 2

Experimental Details

2.1 Substrate Preperation

Using degenerately doped silicon dioxide (SiO_2) wafers that are 270 nm thick as pictured in fig. 2.1 and the subsequent substrate‘s schematic in fig. 2.2, there are several preliminary steps needed prior to device fabrication. For easy indentification of locations on the substrate alignment marks are placed on the wafer using photolithography (see setup in fig. 2.3). There is a main alignment mark pictured in figs. 2.4(a) and 2.4(b) which allows for quicker indentification during electron beam lithography, for example. The alignment marks are in a grid pattern with the coordinate $(0, 0)$ at the center, stretching to $(\pm 6, \pm 6)$ in both the right and left directions. In each of these coordinate locations there smaller alignment marks evenly spaced within them as shown in figs. 2.4(c) and 2.4(d). Next, gold (Au) is deposited on the surface of the wafer, a process that will be explained in more detail in sec. 2.5.

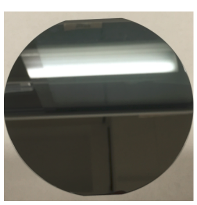

Figure 2.1: Plain, polished uncut Si/SiO_2 wafer.

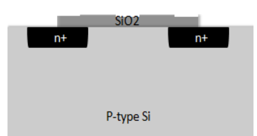

Figure 2.2: Schmatic of Si/SiO_2 substrate.

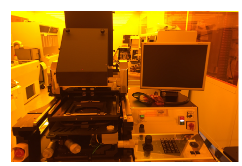

Figure 2.3: Photolithography system for creating alignment marks on substrates.

2.1.1 Substrate Cleaning

First, a SiO_2 wafer is cut to the appropriate size with its preexisting Au layer. To remove the Au layer, the substrate is first soaked in acetone for approximately 5-10 minutes then washed using isopropanol (IPA) and dried with nitrogen (N_2) gas. Next, the substrate in placed in acetone and sonicated for 15 minutes. Then sonicated once more but in IPA this time with a repetition of washing and drying step using IPA and N_2 as described above in between each sonication. In order to remove any remaining organic matter on the surface of the substrate, the substrate is annealed under vacuum at 600°C for 10 minutes and passing forming gas for 2 of the 10 minutes. Forming gas is a mixture of H_2 and an inert gas, usually N_2 [76]. In addition to annealing the substrate for cleanliness, in certain cases when a higher degree of cleanliness is desired the substrate can be treated with oxygen plasma cleaning.

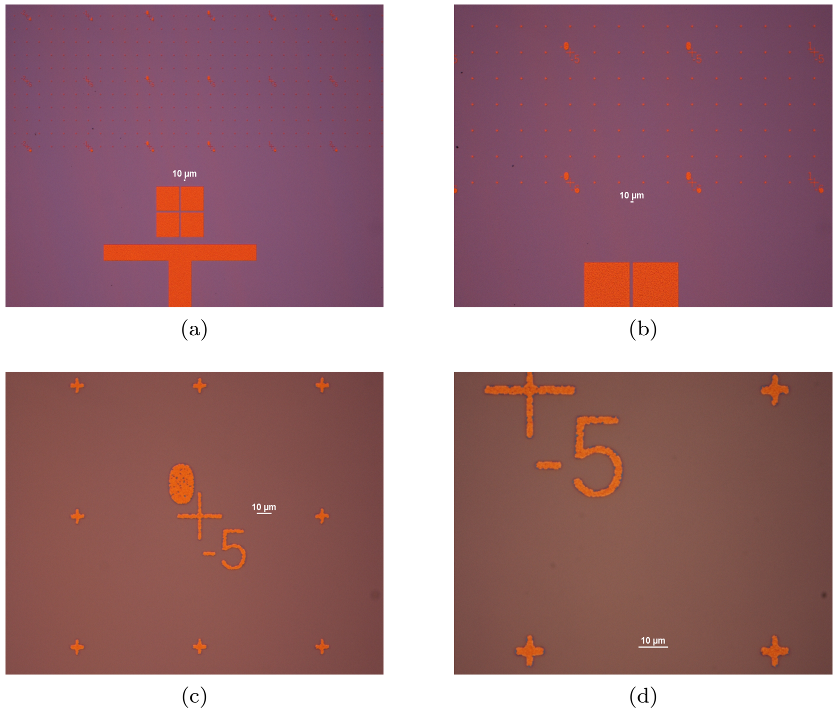

Figure 2.4: (a) Main alignment mark at 5x magnification. (b) Main alignment mark at 10x magnification. (c) Coordinate mark $(0, -5)$ at 50x magnification. (d) Coordinate mark $(0, -5)$ at 100x magnification.

2.2 Exfoliation

To synthesize samples the most common and often most effective method used is mechanical exfoliation, a technique made famous by Novoselov *et al.* [18]. The process involves using Scotch tape to repeatedly cleave layers of MoS_2 or some other TMD. Initially a crystal of a particular TMD (see fig. 2.5(a)) is placed on a piece of Scotch tape (see fig. 2.5(b)). Then taking another piece of tape and pressing in on the crystal that is on the first piece of tape, being sure to press hard and firm on the crystal. The tape is then lifted up and this process is repeated until the whole piece of tape is filled with small samples of the TMD (see fig. 2.5(c)). At the end of this process it is expected that there are a wide range of mixture of sample sizes in terms of area and in term of thickness as well, where thicknesses of $< 3\,\mathrm{nm}$ are not uncommon. To better characterize the samples the optical microscope is used.

The main challenge that exists with this method is the ability to synthesize a high yield of monolayer samples. This does not seem to be much of a challenge when it comes to graphene and some other TMDs, but with regard to MoS_2 this is not the case. Based on recently published literature in an effort to increase the yield of monolayer MoS_2 various methods and techniques were tested and modified accordingly [77]. In this modified method an additional step to cleaning the substrate is added in which it undergoes oxygen plasma cleaning for 10 minutes to ensure the cleanliness of the substrate‘s surface. To promote more bonding between the substrate and the samples, the substrate is first heated at 300° C for 10 minutes without any samples on it. During this process the normal cleaving of sample on tape from crystal takes place. Once the substrate is done heating the tape containing the samples is immediately placed on the substrate and pressed firmly for several minutes. Then the substrate (with the tape still on it) is placed on a glass slide (microscope slide) and is heated at around 85° C for five minutes. Next, the substrate (with tape) is removed from heat and the tape slowly peeled back from the substrate. The result should be a much higher yield of $< 3\,\mathrm{nm}$ samples of larger surface area, and several trilayer, bilayer, and a few monolayer samples.

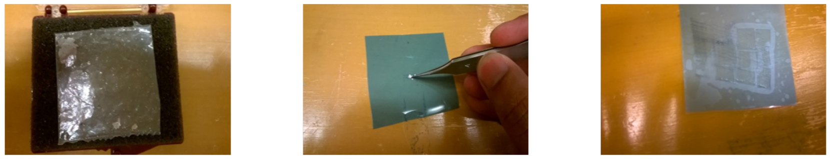

(a) (b) (c)

Figure 2.5: (a) Bulk MoS_2 crystal. (b) Single MoS_2 crystal on tape. (c) Tape with exfoliation MoS_2 crystals.

Most commonly SiO_2 substrates are the main items that are exfoliated onto. However, depending on the material being synthesized, this may not always be the case. In cases where samples of hBN or in the event that the thickness of the synthesized sample is not of great importance and can to tolerated up to $20 - 30\,\mathrm{nm}$, polydimethylsiloxane (PDMS) is exfoliated onto instead of SiO_2 substrates. The resulting samples are of varying thickness, on average around $20\,\mathrm{nm}$. Thin samples (usually trilayer and above) can be made using this method of PDMS, however, these samples tend to have small surface area and lack uniformity which poses problems as to their usability. As such, this remains an effective method for obtaining samples in which thickness is not the main concern. Once the samples have been optically characterized, the sample(s) on PDMS must be transferred to a SiO_2 substrate.

2.3 Device Synthesis

Once the sample or samples have been synthesized and characterized for their specific purpose these samples can begin to be synthesized into a device for measurement. Generally, this involves the technique of transfer. Transfer is usually done using the aforementioned PDMS or using polycarbonate (PC) known as the PC pickup method.

2.3.1 PDMS Transfer

PDMS transfer is most useful for samples that were originally exfoliated onto PDMS, for example hBN . To manufacture PDMS a 10:1 ratio of silicone base and curing agent is mixed together and placed in vacuum for 30 minutes to ensure the removal of any remaining air bubbles. After this time the mixture is then spin coated on a plain SiO_2 wafer and heated at 80° C for 30 minutes then allowed to cool for 30 minutes. Once cooled, the surface of the wafer can be cut using a razor into small stamps that can used for exfoliation and for transfer.

Once the samples that are to be transferred are on the PDMS stamp, it is placed on a glass slide. The optical microscope is used to locate the sample on the stamp and using a razor to cut small excess pieces from the portions of the stamp where the desired sample is not located. This process is repeated until the size of the cut stamp is now reasonably small. The cut stamp is then placed at the edge of a new glass slide with sample area of the stamp as close to the edge as can be and the other side of the stamp is taped down using Scotch tape.

Next a substrate is placed and secured using glue (usually PMMA) to the stage of the transfer setup. The transfer stage setup is pictured in fig. 2.6. It consists of a microscope that has the capability of 10x or 20x magnification and a micro-manipulator. The micro-manipulator is where the glass slide with the PDMS stamp is placed. Using the manipulator the substrate on the stage is approached and the position of the stamp is checked and re-checked multiple times using the microscope to ensure correct overlap of the desired portion of the sample(s). Upon reaching the desired position, the glass slide is lowered, but this time there should be a contrast seen which is the overlapping of the glass slide and the substrate. Once the contrast has enveloped the entire sample that was to be transferred then the manipulator can be used to lift up the glass slide. Once the transfer is complete then the substrate should be annealed at 250° C for 30 minutes in order to remove and residue or orgranic matter that may have remained during the transfer process.

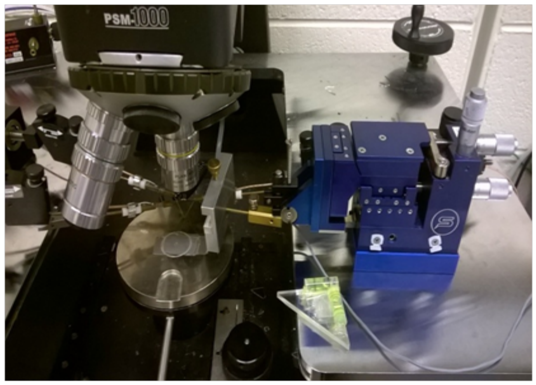

Figure 2.6: Transfer stage setup

2.3.2 Polycarbonate Pickup Method

The PC pickup method is used for samples that have been exfoliated onto a SiO_2 substrate. Generally these are thinner samples with larger surface area that are not as easily obtained by using the PDMS exfoliation method as described in sec. 2.2. To manufacture the PC 3.0 g of chloroform and 0.18 g of polycarbonate resin are put on a plate shaker for about 60 minutes or until the polycarbonate resin have dissolved into the solution.

Next, the substrate that has the sample that is going to be transferred is taped using double-sided tape to a glass slide facing up. Then using a syringe the PC solution is placed in the substrate and evenly spread across it, being sure to locate the area(s) on the substrate where the sample(s) are located, small pre-cut pieces of PDMS are placed over top of these areas. An outline of the PDMS stamps is cut using a razor and any excess PDMS is carefully torn away. Once only the PDMS strips are remaining on the substrate deionized water (DI) is put under the strips in order to create a hydrophobic surface and to ensure that the strip and PC that is trapped underneath it come off the substrate with relative ease. Each strip is placed on its own glass slide and is gently blown with N_2 gas to remove any excess DI from the surface.

Moving to the transfer stage setup and following the steps described in sec. 2.3.1 with regard to using the transfer stage setup. The only difference at this point to using this method as opposed to PDMS transfer is in the final step of the transfer. Instead of only lowering until the contrast change is shown between the region that is desired to be transferred, with PC transfer the entire PC must be lowered down. This is because the PC will be heated before being lifted up. Lowering all the way ensures that all the PC will be melted. Once lowered all the way, the heating device, which is connected to the stage, should be turned up to 130° C. Once this temperature is reached, it should be maintained for approximately two minutes to fully melt the PC film. After heating the substrate and lifting up using micro-manipulator the substrate is placed in chloroform and covered for 30-60 minutes. The purpose of this is to remove any residue left over by the PC film or any other items that may have been introduced at any point in the transfer process. In practice the chloroform soaking generally needs to be repeated several times over a few hours in order to ensure the least amount of remaining residue possible. To confirm the reduction of residue and also characterize the transferred samples an AFM is used.

2.4 Characterization

There are many ways used in modern academia and industry to characterize samples and devices. Some of these methods include scanning tunneling microscopy (STM), transmission electron microscopy (TEM), atomic force microscopy (AFM), and magnetic force microscopy (MFM) [78]. The primary characterization techniques used in this project are AFM and optical characterization.

2.4.1 Optical Characterization

The majority of the optical characterization is carried out using the optical microscope as shown in figs. 2.7(a) and 2.7(b). The microscope can magnify 5x, 10x, 20x, 50x, and 100x, in addition, it can show dark field images.

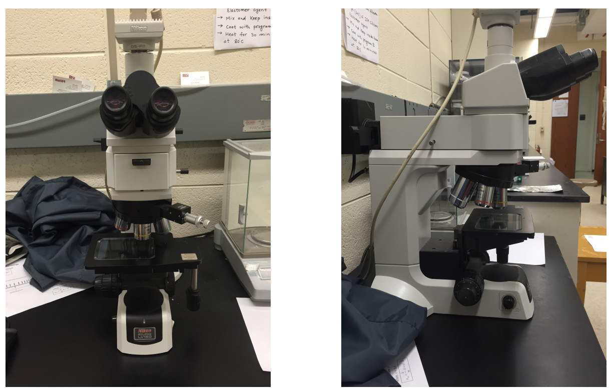

(a) (b)

Figure 2.7: (a) Optical microscope front view. (b) Optical microscope side view.

2.4.2 AFM Characterization

In addition to the characterizing samples optically, AFM characterization is another important aspect of the device design and fabrication process. AFM characterization occurs several times throughout the process, after each transfer of a sample onto another, for example. This occurs for two reasons; to verify the thickness of the sample(s) that have been transferred, and also to verify the cleanliness of the surface of the sample (to ensure that any residue has been removed, especially during the course of PC transfer). Additionally, once the electrodes of the device have been fabricated a final AFM characterization is need to determine the width of the device's channel which is needed to calculate various important electrical properties.

Fig. 2.8(a) shows a front view of the AFM used to characterize. For these purposes, the AFM is operating in "tapping" mode which is less invasive than "contact" mode [78]. In basic terms, an AFM works by measuring the force between the tip of a cantilever (see fig. 2.8(b)) and the sample being imaged.

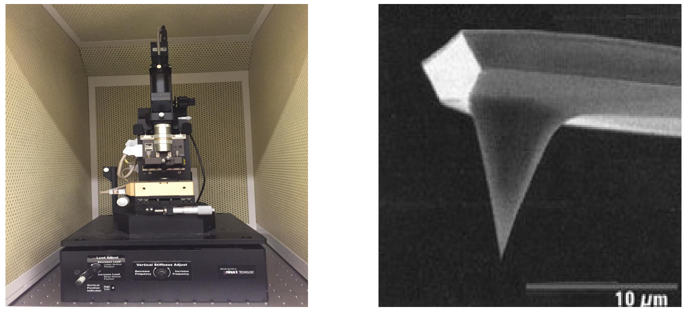

(a) (b)

Figure 2.8: (a) Front view of AFM setup. (b) AFM cantilever tip [79].

2.5 Device Fabrication

In order to perform electrical measurements of devices one must fabricate devices with electrodes. The devices are fabricated according to a specific process, though it is worth noting that under certain circumstances some steps of the process may be omitted or altered, however, the main idea remains the same regardless of the device type being fabricated. Once all transfer steps and samples have been placed in their correct locations the fabrication process begins. This process has three main steps: device design (sec. 2.5.1), electron beam lithography (EBL) (sec. 2.5.2), and metal deposition (sec. 2.5.3).

2.5.1 Device Design

The specifics of device electrode design depends largely on the type of measurement that is desired. For example, fig. 2.10(b) demonstrates a Hall bar device pattern. Despite the varying possibilities of patterns, the method for which the designs are generated remains largely the same. In order to generate these patterns a design software, Nanometer Pattern Generation System (NPGS), is used to draw the electrodes which in turn communicates the designed pattern to the SEM [80].

In preperation for EBL the substrate is spin-coated with two layers of polymethyl methacrylate (PMMA). The first layer of PMMA is 495-A4 is added then the substrate is baked on a hot plate for 5 minutes at 180° C. The first layer is followed by another layer of PMMA, 950-A2 (same polymer of different molecular weight). Again, the substrate is spin-coated with this PMMA layer and baked at the same temperature for 5 minutes.

2.5.2 Electron Beam Lithography

To generate the patterns described in sec. 2.5.1 a SEM is used to complete EBL. Fig. 2.9 shows the control panel and electron beam writer of the SEM. The SEM is optimized by adjusting the beam current to the saturation point. Using the alignment marks mentioned in sec. 2.1 the electron beam is aligned to the correct position on the substrate. The NPGS system allows for adjustments in the concentration of the electron beam current at certain areas, for example, whether a line dose or an area dose is necessary. In general, these values are adjusted as needed depending on the device design but are usually around $300\,\mu\mathrm{C\,cm^{-2}}$ for area doses and $15\,\mu\mathrm{C\,cm^{-1}}$ for line doses. Ultimately, the EBL process creates three separate patterns that are joined together. The first pattern is written at 1000x magnification on the SEM (see fig. 2.10(b)). The second and third patterns (written at 300x and 100x, respectively, see fig. 2.10(a)) are connected to the inner 1000x pattern and they connect this inner pattern to the “electrode pads” where the electrodes will eventually be connected for device measurement. After completing the device pattern, the substrate is developed in a solution of methyl isobutyl ketone (MIBK) and methyl ethyl ketone (MEK) for 70 seconds. The MIBK is the main developer while the MEK acts to enhance the developing process, both fig. 2.10(a) and fig. 2.10(b) have undergone this development process.

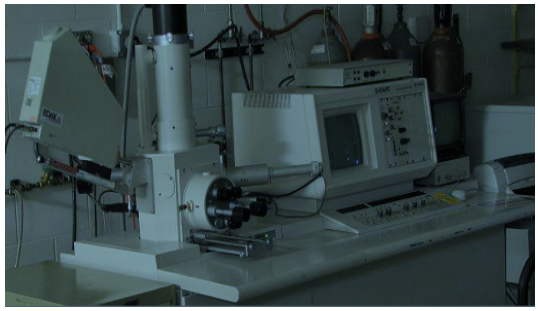

Figure 2.9: Control panel and electron beam writer of scanning electron microscope.

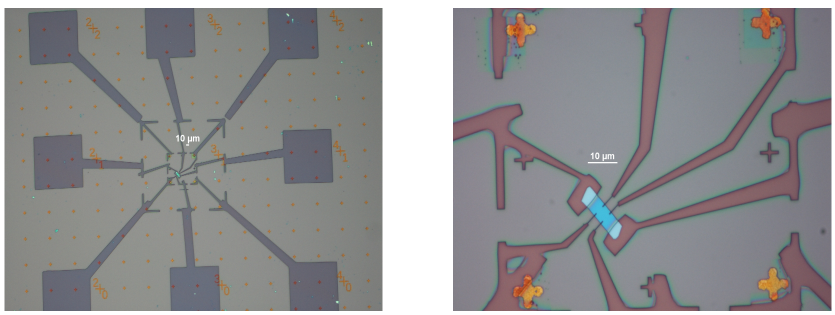

(a) (b)

Figure 2.10: (a) Developed pattern at 10x magnification, (b) developed pattern at 100x magnification. Both developed using MIBK and MEK.

2.5.3 Metal Deposition

In order to make proper electrical contacts metal must be deposited on the pattern made by EBL. This process of metal deposition is done using a Bell Jar deposition (BJD) system which evaporates 10 nm of titanium (Ti) followed by 40 nm of Au on the substrate‘s surface at ultrahigh vacuum ($\sim 10^{-7}$ torr) at a rate of $1\,\text{Å}\,\text{s}^{-1}$. After the metal deposition process is complete, a process called “liftoff” is performed. In this process the substrate is placed in acetone for approximately 5-10 minutes, until the Au has “lifted-off.” Once this process is complete all that remains on the substrate is Au where the EBL was performed. Figs. 2.11(a) and 2.11(b) illustrates a substrate that has undergone the liftoff process, all that remains is the portion of the pattern that is necessary to perform electrical measurements on the device.

2.6 Electrical Measurements and Characterization

Upon completion of the fabrication process and physical characterization processes, the remaining process is electrical characterization. Many of the options available in electrical characterization are put to use, at least in some capacity regardless of the device. Then, depending on the device‘s quality, further measurements can be made in which a more comprehensive electrical data profile can be obtained.

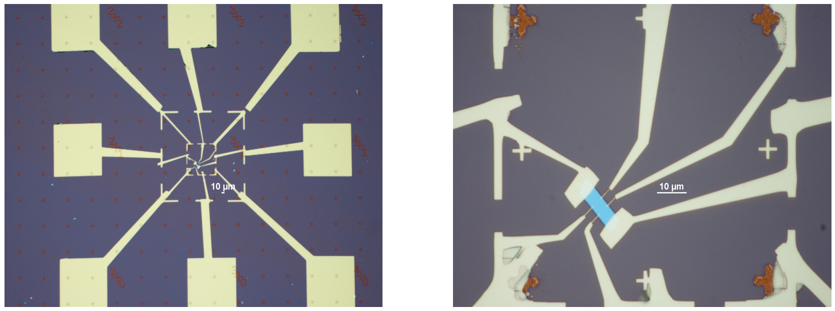

(a) (b)

Figure 2.11: (a) Au/Ti deposited on developed sample after electron beam lithography at 10x. (b) Au/Ti deposited on developed sample after electron beam lithography at 100x.

2.6.1 Measurement Devices

Pictured in fig. 2.12(a) is a measurement device that allows for automated electrical data collection through pre-made programs. The user adjusts parameters and the desired device properties to be measured. Initially, the device is usually measured in non-vacuum conditions at room temperature in order to determine the device‘s quality. If it is determined that the device‘s quality is worth continuing with low temperature measurements then the substrate is placed in the vacuum measurement chamber pictured in fig. 2.12(b). This apparatus is used in conjuction with the measurement setup in fig. 2.12(a) to continue measurements. However, in this configuration the measurements take place under ultrahigh vacuum ($\sim 10^{-6}$ to 10^{-7} torr) and temperature control via liquid nitrogen (with the ability to cool to 70 K). In addition, there is another measurement device that allows for both temperature control and the application of a magnetic field. This device, known as a physical property measurement system (PPMS), is shown in fig. 2.12(c) and is used in situations when it is necessary to apply a magnetic field such as measuring a Hall device.

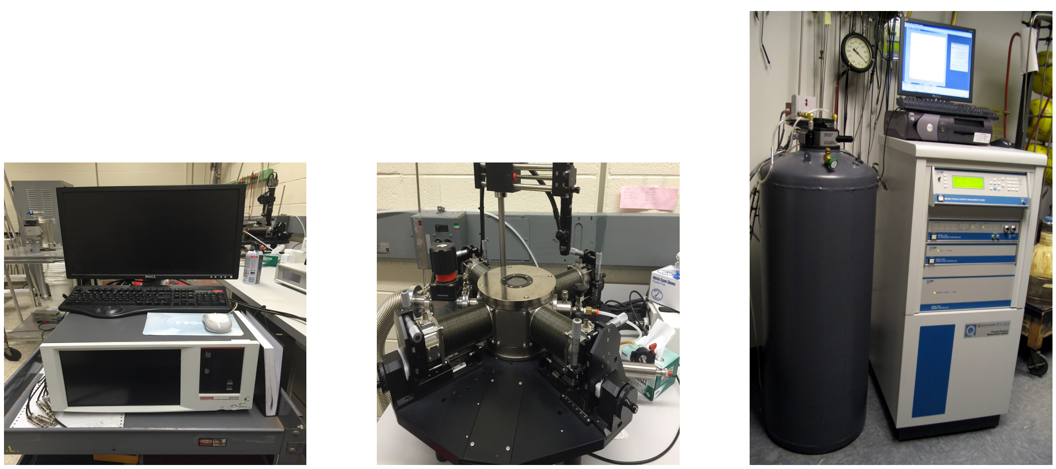

(a) (b) (c)

Figure 2.12: (a) Keithley semiconductor measurement system. (b) Low temperature, vacuum measurement chamber. (c) Physical property measurement system.

Chapter 3

Intrinsic Properties and Scattering Mechanisms

At present, much of the problems that remain in the TMD and heterostructure community are centered around the improvement of device performance and determining the limiting factors of such devices. As such, in order to overcome these hurdles some new innovative techniques have been introduced. One of these is the problem of making quality metal/semiconductor contacts, several approaches exist for attempting to reconcile this, however, the approaches do not seem to be universal for all types of TMDs. Coming up with a solution to this problem ultimately allows for the further understanding of some of the other remaining problems, such as device mobility limits. This has been of much debate in the community and first principles calculations predict values higher than what has so far been reported experimentally, suggesting room for improvements. To improve mobility, it must first be understood what factors limit the mobility. However, to do this the contact resistance must be low otherwise one cannot examine the intrinsic channel properties with high-resistance contacts. Ultimately, these concerns and their solutions are fueled by the desire feasibility in device applications. This aspect leads to another factor of concern, how doping effects the mobility and device performance. Inventing novel approaches to these problems will, in the future, lead to better TMD devices and eventual applications.

3.1 Approach to Low-Resistance Contacts

Developing low-resistance contacts is important two enable the study of intrinsic transport properties of devices, but also it is vital to applications of TMDs. Large contact resistance at room temperature is not ideal for applications. At the metal/semiconductor contact interface a barrier develops, the SB [81]. The device in question must be able to supply the necessary current, and the voltage drop across the contacts should be small compared to the voltage drop across the device's active channel region. In most cases, the contacts should be ohmic, the current-voltage characteristic should be linear and not degrade the device's performance to any significant extent [82]. In the ideal, theoretical case (Schottky-Mott model) the SBH is given by

$$\Phi_{\mathrm{B}p} = \frac{E_g}{e} - (\Phi_m - \chi_s)\,, \tag{3.1}$$

where $\Phi_{\mathrm{B}p}$ is the hole barrier height, e is the charge of an electron, E_g is the semiconductor bandgap energy, Φ_m is the metal workfunction, χ_s is the semiconductor electron affinity, note that these properties are intrinsic to the material before forming the junction [83]. In reality the description is not this simple and is largely dependent on other factors, such as imperfections, Fermi level pinning, and Fermi level mismatch [84]. For a metal/p-type semiconductor interface the magnitude of the SBH is reflective of the mismatch in Fermi level of the metal and the valence band maximum (VBM) of the semiconductor. Conversely, for the case of a metal/n-type interface it is the mismatch in the Fermi level of the metal and the conduction band minimum (CBM) of the semiconductor [85]. Therefore, to address the issue of contact resistance one must find ways to effectively "tune" the SB.

There have been several approaches employed in order to reduce the contact resistance. One method is to attempt to tune the SBH by using different common metals to find a desirable work function. Eq. 3.1 implies that the SBH is linearly dependent on the work function Φ_m of the metal. However, in reality, this is usually not the case because, one, finding metals with the proper work function that minimizes the SBH while still maintaining high conductivity has proven to be difficult, and, two, the lowering that would potentially be achieved by the use of the proper work function would most likely be diminished due to Fermi level pinning [61, 62, 86]. Fermi level pinning occurs when there are surface states that develop in the bandgap and pin the Fermi level position of the semiconductor [85]. Another method is the use of graphene contacts [87, 88, 89]. Barrier-free contacts have been achieved using this method in combination with MoS_2 using a gate potential to tune band alignment [90]. However, this method has not been shown to be extendable down to low enough contact resistances in some other TMDs, most notably WSe_2, but has been shown to be tunable down to ($< 2\,\mathrm{k}\Omega\,\mu$m) [91, 87]. The method to that is enacted here to reduce the contact resistance is using degenerately doped contact regions. By degenerately doping the contact region one can thin the SB width. However, this method is not without its challenges as well. Several doping techniques that can be used have limited spatial resolution [68]. Depsite the challenges posed, this method has produced promising results that are transferrable to TMDs including WSe_2, MoS_2, and $MoSe_2$ resulting in high-performance, low contact resistance devices.

To determine the contact resistance of fabricated devices a method known as transmission line model (TLM) is used. In general, resistance is given by

$$R = \frac{\rho}{A} l, \tag{3.2}$$

where, in this case, it is assume that the resistivity ρ and the area A of the electrodes are constant throughout the device [92]. The resistance R is then proportional to the length of the channel l. By determining the resistance as a function of length one can deduce the contact resistance. The total contact resistance is given by

$$R = R_{\mathrm{ch}} + 2R_{\mathrm{c}}, \tag{3.3}$$

where R_{c} and R_{ch} are the contact and channel resistances, respectively [92]. A typical device for a TLM measurement has drain and source electrodes with varying lengths between them. By find the resistance from the gradient of an IV characteristic curve, one can apply the logic from eqs. 3.2 and 3.3 to find the contact resistance. The contact resistance is ultimately extracted from the y-intercept of a linear fit of resistance as a function of length for the device. In general, this method is done at several temperatures to further characterize the quality of the contacts as one would expect that at low temperatures, for low-resistance contacts, they would behave in similar fashion as they did at higher temperatures. To determine the affect that varying doping schemes has on contact resistance devices that were lightly doped ($Nb_{0.0005}W_{0.9995}Se_2$) were measured using TLM and compared to degenerately doped devices ($Nb_{0.005}W_{0.995}Se_2$).

3.1.1 Transmission Line Method: $Nb_{0.0005}W_{0.9995}Se_2$

As stated in sec. 3.1, the TLM measurement involves designing a device that has varying drain source channel lengths in order to determine the resistance as a function of length. Fig. 3.1(a) shows an optical micrograph consisting of a lightly doped WSe_2 ($Nb_{0.0005}W_{0.9995}Se_2$) channel. Figs. 3.1(b)-3.1(d) show the total resistance as a function of length for both $V_{bg} = 0\,\mathrm{V}$ and $V_{bg} = -60\,\mathrm{V}$ at room temperature. The contact resistance are then determine from the linear fit and the y-intercept. These figures show ohmic contacts with a minimum contact resistance of $R_{\mathrm{c}} = 2.35\,\mathrm{k}\Omega\,\mu$m achieved with application of $V_{bg} = -60\,\mathrm{V}$.

In addition, the contact resistances are lower for the higher values of V_{bg}. This is due, in part, to the fact that the higher V_{bg} works to reduce the width of the SB and allow for more transmission across the barrier that has developed between the metal/semiconductor interface. Moreover, when there is no V_{bg} applied, the reported contact resistances are an order of magnitude higher. The fact that the channel material in use here is only lightly doped means that there is a larger mismatch between the Fermi level of the metal and the VBM causing a larger SBH than one would expect with a channel that was more heavily doped.

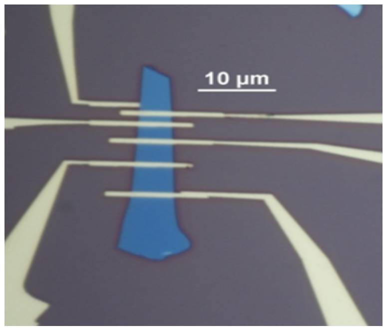

(a)

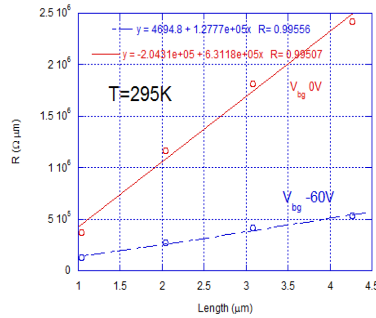

(b)

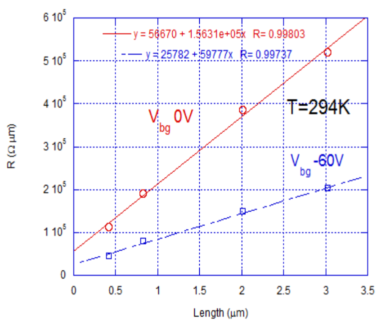

(c)

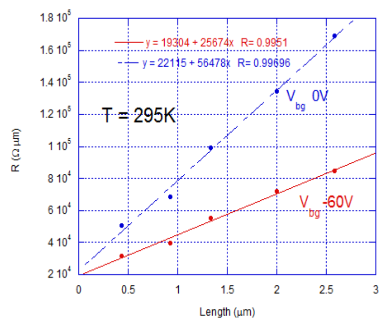

(d)

Figure 3.1: (a) Optical micrograph of a device structure for TLM measurement consisting of lightly p-doped WSe_2 ($Nb_{0.0005}W_{0.9995}Se_2$) with Ti/Au metal contacts. (b)-(d) Normalized total resistance as a function of channel length measured at room temperature.

3.1.2 Transmission Line Method: $Nb_{0.005}W_{0.995}Se_2$

The lightly doped WSe_2 device showed reasonably low contact resistances at room temperature, but lower-resistance contacts are desired. Using TLM degenerately doped WSe_2 ($Nb_{0.005}W_{0.995}Se_2$) devices were measured. Fig. 3.2(a) shows an optical micrograph of the device design which identical to that in sec. 3.1.1. The contact resistances as a function of length are shown in figs. 3.2(b) and 3.2(c) at room temperature and 5 K, respectively. At both temperatures they exhibit linear ohmic behavior. Even more promising is that the values for contact resistance are essentially the same at high and low temperature, which indicates significant reduction of the SB. The low temperature performance means that the contacts are of high quality as the contacts tend to degrade as temperature decreases mainly due to the lack of thermionic emmission of carriers [85].

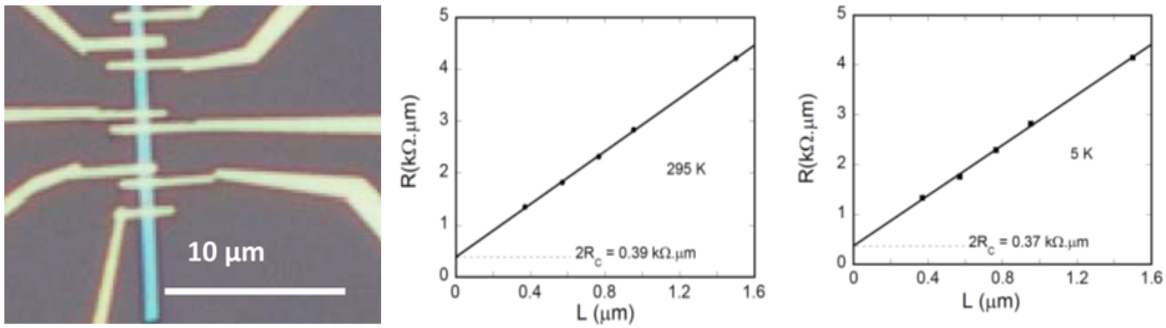

(a) (b) (c)

Figure 3.2: (a) Optical micrograph of a device structure for TLM measurement consisting of degenerately p-doped WSe_2 ($Nb_{0.005}W_{0.995}Se_2$) with Ti/Au metal contacts. (b) Normalized total resistance as a function of channel length measured at room temperature $T = 295\,\mathrm{K}$ and (c) low temperature $T = 5\,\mathrm{K}$. Figures appeared in ref. [91].

3.1.3 Discussion of Results for Light and Degenerately Doped Contacts

The results for lightly ($Nb_{0.0005}W_{0.9995}Se_2$) and degenerately ($Nb_{0.005}W_{0.995}Se_2$) doped WSe_2 contacts are summarized in table 3.1. The degenerately doped contacts have resistances of at least an order of magnitude lower at room temperature due to the lowered SBH from the higher doping scheme. The lightly doped contacts, though still relatively high, demonstrate the effect that applying a higher V_{bg} can have on the SB. An effective thinning of the barrier is observed for higher backgate voltage and thus this can also be used to further tune the SB and lower contact resistances. The results from the lightly doped WSe_2 channel are on the same order of magnitude as what has been previously shown using graphene/WSe_2 contacts ($\sim 2\,\mathrm{k\Omega}\,\mu\mathrm{m}$) [87]. The results shown obtained for the degenerately doped WSe_2 are significantly lower than graphene/WSe_2 method and are in line with the best results that have been achieved for TMDs ($\sim 0.2 - 0.7\,\mathrm{k\Omega}\,\mu\mathrm{m}$) [93, 67, 94]. With these results in mind, this 2D/2D contact method using degenerately doped WSe_2 ($Nb_{0.005}W_{0.995}Se_2$) looks to be a viable and effective way to engineer low-resistance contacts which will be essential to explore the intrinsic channel properties of TMDs, the performance limits, and also when it comes to applications.

Doping Content	Temperature (K)	$R_\mathrm{c}(\mathrm{k\Omega}\,\mu\mathrm{m})^*$
(0.05%) $Nb_{0.0005}W_{0.9995}Se_2$	295	$2.35^\dagger$
(0.05%) $Nb_{0.0005}W_{0.9995}Se_2$	294	$12.9^\dagger$
(0.05%) $Nb_{0.0005}W_{0.9995}Se_2$	295	$9.65^\dagger$
(0.5%) $Nb_{0.005}W_{0.995}Se_2$	295	$0.195^\ddagger$
(0.5%) $Nb_{0.005}W_{0.995}Se_2$	5	$0.185^\ddagger$

* The contact resistances R_c are reported as per electrode by taking the intercept and dividing by 2. In some other references this may not be the case.
† Resistance values from figs. 3.1(b), 3.1(c), and 3.1(d).
‡ Resistance values from figs. 3.2(b) and 3.2(c).

Table 3.1: Summary of contact resistances for lightly p-doped WSe_2 ($Nb_{0.0005}W_{0.9995}Se_2$) and degenerately p-doped WSe_2 ($Nb_{0.005}W_{0.995}Se_2$) found using linear fit data from figs. 3.1(b)-3.1(d) and 3.2(b)-3.2(c).

3.2 Field-Effect Mobility and Scattering Mechanisms

There are several properties to electrically characterize and quantify the performance of a device. One such property is the two-probe and four-probe field-effect mobility μ_{FE}. The two-probe field-effect mobility is given by

$$\mu_{\mathrm{FE}} = \frac{L}{w}\frac{1}{C}\frac{1}{V_{ds}}\frac{dI_{ds}}{V_{bg}}, \tag{3.4}$$

where L is the length of the channel (the distance between the source and drain), w is the width of the channel, I_{ds} is the drain current, V_{bg} is the backgate voltage, V_{ds} is the drain voltage, and C is the geometric capacitance [95]. To measure the field-effect mobility there are two main approaches used, either the two-probe method or the four-probe method. The two-probe method is shown in fig. 3.3(a). In this configuration measurement takes place between the drain and source only. The main drawback of this measurement is that it is subject to resistance that can make data difficult to interpret because of this [92]. Alternatively, there is the four-point probe configuration which is shown in fig. 3.3(b) [96]. The main advantage of this configuration is that the voltage drop is measured across V_3 and V_2 and therefore allows the resistance to be subtracted. The field-effect mobility is important to characterizing a device because, it can reveal information about scattering mechanisms present and how they affect the mobility. Also, depending on the device's channel and whether it is doped or not, the mobility shows how the doping can be tuned to perform in a desired manner for device applications, especially at room temperature. To begin to study these issues devices with varying doping schemes and fabrication methods were measured to address where improvements can be made and where unknowns still exist.

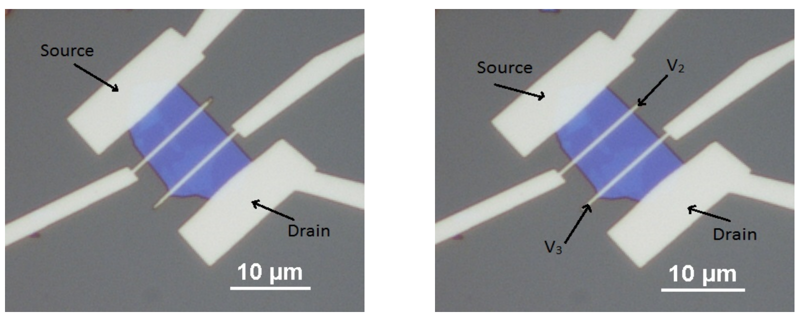

(a) (b)

Figure 3.3: Examples of (a) two-point probe measurement configuration for field-effect mobility measurements and (b) four-point probe configuration.

3.2.1 Applying Low-Resistance Contacts: Doped Channel

It is important to understand the how doping affects the mobility of a device, especially for device applications. To study this, device's with were fabricated using the method outlined in figs. 3.4(a)-3.4(d). A piece of hBN is first transferred onto the Si/SiO_2 substrate. This is done because hBN is smoother than the plain Si/SiO_2 substrate and acts to reduce and effectively eliminate the majority of substrate and roughness scattering that would be present otherwise. Next, the channel is transferred onto the hBN substrate, in this case $Nb_{0.0001}W_{0.9999}Se_2$ (fig. 3.4(a)). This is followed by another piece of hBN which acts to cover the channel and protect it from external effects (fig. 3.4(b)). The degenerately doped contacts are added and cover the remaining exposed pieces of the channel for the reasons outlined in sec. 3.1 (fig. 3.4(c)). Electrodes are fabricated on the device in order to perform a two-probe measurement (fig. 3.4(d)).

The device was characterized first without annealing the device. Figs. 3.5(a) and 3.5(b) show the IV characteristic curves at $T = 300\,\mathrm{K}$ and $T = 10\,\mathrm{K}$, respectively. Ohmic contacts are observed at high temperature, however, at low temperature the curve becomes nonlinear indicating a non-ohmic behavior.

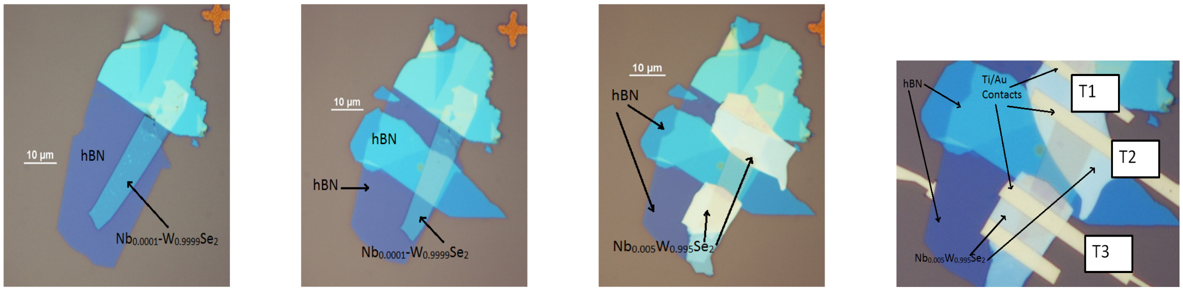

(a) (b) (c) (d)

Figure 3.4: (a) $Nb_{0.0001}W_{0.9999}Se_2$ transferred to hBN substate, (b) top hBN transferred onto channel, (c) degenerately doped ($Nb_{0.005}W_{0.995}Se_2$) contacts transferred onto device, and (d) device after fabrication steps with Ti/Au metal electrodes consisting of a 5.6 nm thick channel.

Additionally, fig. 3.5(c) shows the field-effect mobility as a function of temperature. The behavior is that of increasing mobility with decreasing temperature, however, there is a deviation in the mobility for $V_{ds} = -50\,\mathrm{mV}$ as compared to $V_{ds} = -1\,\mathrm{V}$ at low temperatures. One would expect the two curves to be relatively identical. In an effort to improve the device's properties, the device was annealed for 30 minutes

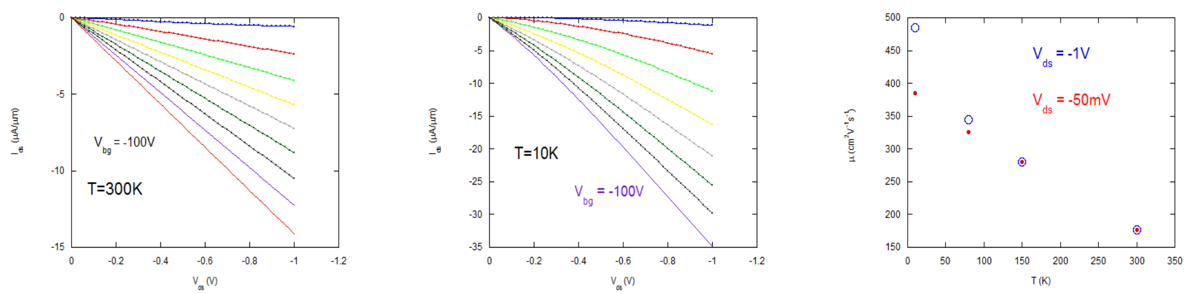

(a) (b) (c)

Figure 3.5: (a) IV chacteristics of device at $T = 300\,\mathrm{K}$ and (b) at $T = 10\,\mathrm{K}$. (c) Two-terminal field-effect mobility as a function of temperature for $V_{ds} = -50\,\mathrm{mV}$ and $-1\,\mathrm{V}$. *Note: figures correspond to device shown in fig. 3.4(d). Measurements shown were made before the device was annealed.*

at 250° C. During the process of annealing some of the organic matter that is affecting the device at lower temperatures is hoped to be removed and thus improving the device's performance [97]. Figs. 3.6(a) and 3.5(b) show the IV characteristic curves for the device after it has been annealed. It shows the previously observed ohmic behavior at high temperature, while it also shows a corrected behavior at low temperature with less delineated behavior. As a result, in fig. 3.6(c) one observes slightly improved mobility values at lower temperatures and there is no longer a deviation at low temperature for the two V_{ds} values.

3.2.2 Applying Low-Resistance Contacts: Undoped Channel

In addition to determining how the doping of channel material affects its properties, the contact method from sec. 3.1 was also applied to an undoped channel to determine its field-effect mobility and how well the new contact method can improve the performance. Using the same method as was for the doped channel ($Nb_{0.0001}W_{0.9999}Se_2$) device in subsec. 3.2.1 using a hBN substrate and degenerately doped ($Nb_{0.005}W_{0.995}Se_2$) contacts with a hBN cover and a few-layer, undoped WSe_2 channel as shown in

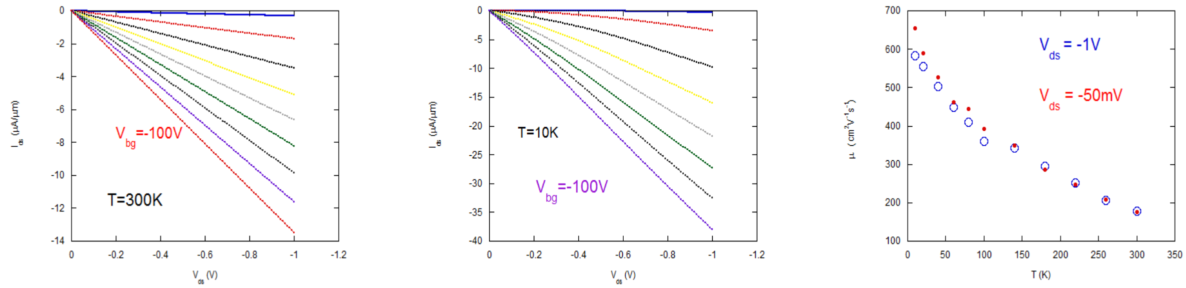

(a) (b) (c)

Figure 3.6: (a) IV chacteristics of device at $T = 300\,\mathrm{K}$ and (b) at $T = 10\,\mathrm{K}$. (c) Two-terminal field-effect mobility as a function of temperature for $V_{ds} = -50\,\mathrm{mV}$ and $-1\,\mathrm{V}$. *Note: figures correspond to device shown in fig. 3.4(d). Measurements shown were made after the device was annealed for 30 minutes at* 250° C.

fig. 3.7(a). The quality of the contacts for the device are appartent in the inset of fig. 3.7(c) as the IV curves are linear at $T = 5\,\mathrm{K}$. The conductivity as a function of backgate voltage V_{bg} is pictured in fig. 3.7(b) for various temperatures. It shows results consistent with expectation, the mobility increases with V_{bg} and mobility also increases with decreasing temperature. Furthermore, the filed-effect mobility is shown in fig. 3.7(c) showing increasing mobility with decreasing temperature, consistent with expectation.

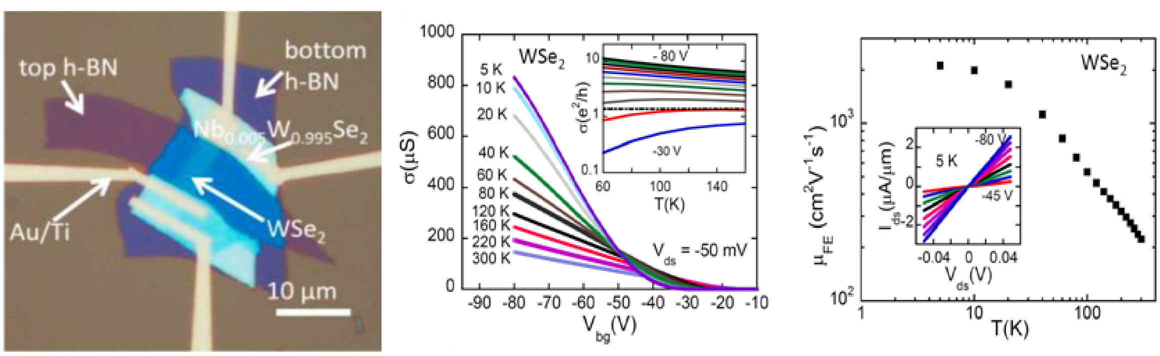

(a) (b) (c)

Figure 3.7: (a) Optical micrograph of WSe_2 FET with degenerately p-doped WSe_2 ($Nb_{0.005}W_{0.995}Se_2$) contacts with channel region on hBN substrate and covered with a top hBN piece. (b) Temperature dependent two-terminal conductivity as a function of V_{bg} at $V_{ds} = -50\,\mathrm{mV}$ for device shown in (a). (c) Two-terminal field-effect mobility. Figures appeared in ref. [91].

3.2.3 Discussion of Two-Probe Measurement Results in Doped and Undoped Channels

The results of field-effect mobility measurements using a lightly doped ($Nb_{0.0001}W_{0.9999}Se_2$) channel with degenerately doped channel show a $T = 300\,\mathrm{K}$ field-effect mobility $\mu_{\mathrm{FE}} = 180\,\mathrm{cm^2V^{-1}s^{-1}}$. This value is on the same order of magnitude as previously measured results using p-doped, few-layer WSe_2 device.

Pradhan *et al.* reported a maximum mobility of $\mu_{\mathrm{FE}} = 350\,\mathrm{cm}^2\mathrm{V}^{-1}\mathrm{s}^{-1}$ at the same temperature. In addition, the low temperature mobilities are also consistent with previous results where $\mu_{\mathrm{FE}} = 650\,\mathrm{cm}^2\mathrm{V}^{-1}\mathrm{s}^{-1}$ at $T = 150\,\mathrm{K}$ compared to our $\mu_{\mathrm{FE}} = 350\,\mathrm{cm}^2\mathrm{V}^{-1}\mathrm{s}^{-1}$ at the same temperature [98]. The mobility measurements show that, in general, the mobility at high temperatures is dominated by phonon scattering [99]. This effect is diminished as the temperature is increased and the scattering becomes primarily due to Coulomb scattering and impurities. Therefore, one can deduce that by changin the doping content of the channel coupled with the use of the new contact method mobility can be tuned with the right approach, which is useful when it comes to applications. The ability to demonstrate low-resistance 2D/2D contacts is important. It enables the investigation of the intrinsic channel properties of the device, namely how the scattering mechanisms effect the mobility. A better understanding of how these mechanisms work leads to a further understanding of how the device performance can be improved.

3.3 Hall Effect and Applying Low-Resistance Contacts

The field-effect mobility μ_{FE} is one quantity to characterize the quality of a device. Another widely used quantity is the Hall mobility μ_H. The Hall mobility is measured using the Hall effect. This quantity is useful because it directly gives several values that are not readily calcuable from using the field-effect mobility, such as resistivity ρ, mobility μ, and (charge) carrier density n [92]. Consider the setup shown in fig. 3.8, where L is taken to be in the x-direction, width w in the y-direction, thickness t in the z-direction, and e denotes a charge carrier which can either be an electron or a hole. The current I flows in the positive x-direction and is given by

$$I = Jwt = nev_x wt, \tag{3.5}$$

where J is the current density in the x-direction, n is the charge carrier number density, and v_x is the charge carrier drift velocity in the positive x-direction. The current I is a result of the application of an electric field E_x along the positive x-direction. In the presence of a magnetic field B applied in the positive z-direction the charge carrier will experience a Lorentz for that deflects them towards one side of the device. As a result there is an accumulation of charges along one side of the device which in turn creates a transverse electric field E_y [100]. This transverse electric field is given by

$$E_y = v_x B. \tag{3.6}$$

The accumulation of charges on one side of the device creates a potential differnece that is related to the this transverse electric field and be used to find the Hall voltage V_H by integrating across the width of the device to arrive at

$$V_H = -\frac{IB}{t}\left(\frac{1}{ne}\right). \tag{3.7}$$

From eq. 3.8 the Hall coefficient is found to be

$$R_H = \frac{1}{ne} = \frac{V_H t}{IB}. \tag{3.8}$$

Since e refers to either electrons or holes, the sign of R_H would also vary in accord with the proper carrier being described in the given circumstance. Furthermore, the conductivity is given by

$$\sigma = ne\mu_H, \tag{3.9}$$

where σ is the conductivity and μ_H denotes the Hall mobility. Thus, an expression for the Hall mobility can be found by combining eqs. 3.8 and 3.9 to give

$$\mu_H = |R_H|\sigma = \frac{\sigma V_H t}{IB}. \tag{3.10}$$

As stated above, the result from eqs. 3.8 and 3.10 give a direct relation using measurable and calcuable quantities to the carrier density, resistivity ($\rho = \sigma^{-1}$), and the hall mobility. Using this method, one can further characterize a device's behavior to better understand the mechanisms that control and limit the performance at high and low temperatures as well as the effects of doping the channel, and how this information can be used to further improve the performance of the device.

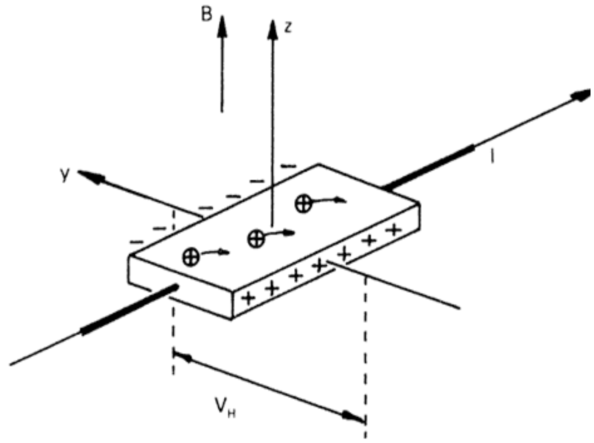

Figure 3.8: Geometry of Hall effect measurement. Current flows in the positive x-direction and magnetic field is applied in the positive z direction generating a Hall voltage [101]. Diagram originally appeared in ref. [102].

3.3.1 Hall Effect: $Nb_{0.0005}W_{0.9995}Se_2$

In order to perform the Hall measurement the device design is important. There need to be electrodes that are properly aligned parallel to one another in order to measure the longitudinal conductance (resistivity $\rho_{xx} = \sigma_{xx}^{-1}$) σ_{xx} and the transverse conductivity (resistivity $\rho_{xy} = \sigma_{xy}^{-1}$) σ_{xy} (the conductivity used to measure the Hall mobility). Fig. 3.9 shows an optical micrograph of the design used for the Hall measurement in this case. Note that the channel material used here was lightly doped WSe_2 ($Nb_{0.0005}W_{0.9995}Se_2$). Fig. 3.10(a) shows the IV characteristic curve of the device as a function of V_{ds} for several backgate voltages at $T = 300\,\mathrm{K}$. This shows that the device exhibits linear and ohmic contacts at this temperature. Fig. 3.10(b) shows the conductivity σ as a function of backgate voltage V_{bg} for various temperatures. The trend shown, conductivity increasing as temperature increases for the same V_{bg}, is not what is expected to occur. Instead, the conductivity should increase with decreasing temperature. The fact that this device exhibits this behavior points to the development of some barrier that degrades the device's performance. This is further confirmed in fig. 3.10(c) where the Hall mobility μ_H as a function of V_{bg} for various temperatures is shown. Again, one would expect that as temperature is increased, the mobility would decrease. However, the reserve is true in this device. There are several reasons for this. Phonon scattering can be ruled out as a cause, because that is primarily temperature dependent and its effect would decrease with decreasing temperature raising the mobility. Therefore, the resulting degradation of mobility here are due to Coulomb scattering, surface and roughness scattering, and impurities introduced from doping the channel and the lack of a hBN channel cover. Fig. 3.10(d) illustrates the Hall mobility as a function of charge carrier densities $n = -3.5 \times 10^{-7}\,\mathrm{C\,cm^{-2}}$ and $n = -2.5 \times 10^{-7}\,\mathrm{C\,cm^{-2}}$. As charge carrier density is increased through the increase of V_{bg} the mobility increases due to more the introduction of more carriers. In addition, in principle one would expect that for a given V_{bg} the carrier density should be the same across all temperatures. More specifcally, fig. 3.10(e) should show the points all along the same line, however, there is some discrepancy. The slope of this curve would give the capacitance and the expectation is that the value would be the same within some relative error, but the lack of this fact points to some device defects that need to further improved upon.

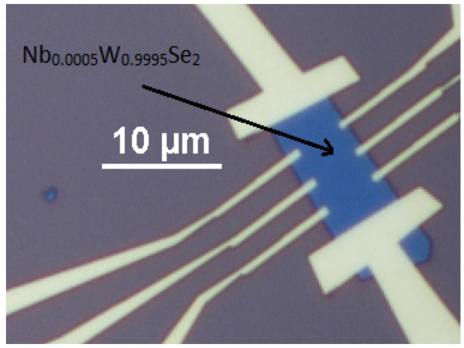

Figure 3.9: Optical micrograph of device structure consisting of lightly p-doped WSe_2 ($Nb_{0.0005}W_{0.9995}Se_2$) with device thickness 7.7 nm and Ti/Au metal contacts.

3.3.2 Hall Effect: Discussion and Improvements

The Hall mobilities reported using this lightly doped ($Nb_{0.0005}W_{0.9995}Se_2$) device range from $\mu_H = 31.9\,\mathrm{cm^2V^{-1}s^{-1}}$ at $T = 300\,\mathrm{K}$ to $\mu_H = 16.7\,\mathrm{cm^2V^{-1}s^{-1}}$ at $T = 180\,\mathrm{K}$. Compared to literature values for few-layer p-type WSe_2 Hall mobilities, these values are an order of magnitude lower [98]. Several improvements, however, can be made to the device fabrication that can readily improve the observed mobility. First, the use of a hBN substrate instead of Si/SiO_2 substrate would reduce the likelyhood of scattering due to roughness and interface effects between it and the channel. Second, the use of a hBN cover over the channel would also decrease any external effects and protect the channel. Finally, and most importantly, applying the 2D/2D contact method would improve the mobility of the device across all temperatures.

In addition to using the doped channel material, with the use of the 2D/2D contact method, it is hopeful to reach high-quality devices in the bilayer and multilayer regimes. Previously measured results have shown other TMDs can achieve high mobilities reaching $34,000\,\mathrm{cm^2V^{-1}s^{-1}}$ using graphene contacts [75]. For reasons stated before in sec. 3.1 this is not viable for WSe_2. This goal in both p and n-type WSe_2 is desired because it would ultimately lead to the ability to study the quantum transport properties that are not readily attainable with device's of lesser quality. However, this poses many challenges such as fabricating devices that have high mobilities ($> 10^3\,\mathrm{cm^2V^{-1}s^{-1}}$) at low temperatures ($< 4\,\mathrm{K}$).

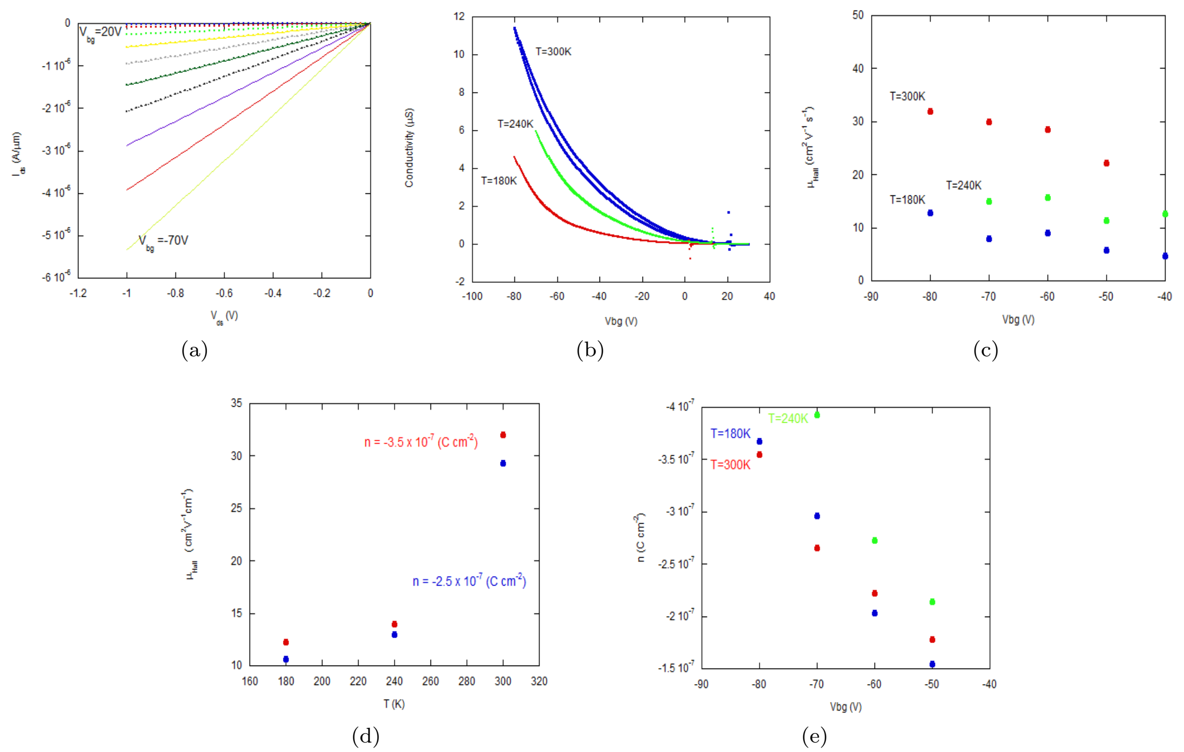

Figure 3.10: (a) IV characteristic curve at $T = 300\,\mathrm{K}$ as a function of V_{ds} for V_{bg} ranging from $-70\,\mathrm{V}$ to $20\,\mathrm{V}$. (b) Temperature-dependence of conductivity and (c) Hall mobility as a function of V_{bg}. (d) Charge carrier denisty dependence of Hall mobility as a function of temperature and (e) temperature dependence of charge carrier density as a function of V_{bg}. *Note: the data here corresponds to device shown in fig. 3.9.*

Chapter 4

Future Works and Conclusion

Certain measurable quantities are valued because of the information they reveal about the geometry of the Fermi surface. Additionally, these quantities are attractive because they depend only on universal constants, experimentally controlled variables, and information about the electronic band structure which is entirely determined by the shape of the Fermi surface [103]. These measurable quantities commonly arise in the presence of a strong magnetic field and low temperature system. Determining the Fermi surface geometry provides insight into the transport and scattering properties of the material.

4.1 Integer Quantum Hall Effects

In a two-dimensional electron system (2DES) there are a number of interesting phenomena that occurs at low temperatures in the presence of strong magnetic fields. One such effect is the integer quantum Hall effect (IQHE). The IQHE was discovered in 1980 by Klitzing *et al.* [104]. They showed that under a quantum regime of temperature and magnetic field there is a quantization of the Hall resistance, which deviates from its linearity in the magnetic field seen in the classical Hall effect, displaying plateaus at particular values of the magnetic field where the Hall resistance is given purely in terms of universal constants. In addition, the plateaus observed in the Hall resistance are accompanied by a vanishing longitudinal resistance [104, 99, 105, 106].

In order to fully mathematically describe the theory behind the IQHE one must first introduce the concept of Landau levels. Here we assume a quantum regime in which there is a low temperature and high magnetic field such that $\hbar\omega \gg k_B T$. The Hamiltonian of a particle in a uniform magnetic field is given by

$$\hat{H} = \frac{1}{2m}\left(\hat{p}_x + eBy/c\right)^2 + \frac{\hat{p}_y^2}{2m} + \frac{\hat{p}_z}{2m} - \left(\mu/s\right)\hat{s}_z B, \tag{4.1}$$

where $\hat{p}_i$ is the momentum operator in the specified coordinate direction, B is the magnetic field, e is the charge of an electron, $\left(\mu/s\right)\hat{s}_z$ is the intrinsic magnetic moment operator [107]. It is worth noting that the vector potential chosen in eq. 4.1 is known as the Landau gauge, $\vec{A} = (-By, 0, 0)$, which implies the magnetic field B is directed in the positive z-direction [108, 109]. In this case the eigenfunctions of the Hamiltonian must take the form,

$$\psi\left(\vec{r}\right) = e^{(i/\hbar)(p_x x + p_z z)}\chi\left(y\right), \tag{4.2}$$

where $\chi\left(y\right)$ is defined by solutions to

$$\frac{\partial^2\chi}{\partial y^2} + \frac{2m}{\hbar^2}\left[E + \left(\mu/s\right)\sigma B - \frac{p_z^2}{2m} - \frac{1}{2}m\left(\frac{eB}{mc}\right)^2\left(y - y_0\right)^2\right]\chi = 0, \tag{4.3}$$

where $y_0 = -cp_x/eB$ and $\omega = |e|B/mc$. Additionally, since the Hamiltonian does not explicitly depend on x and z this implies that both the x and z components of the generalized momentum are conserved. Eq. 4.3 is formally identical to that of the linear oscillator, thus the expression for the energy levels of a particle in a uniform magnetic field is

$$E = \left(n + \frac{1}{2}\right)\frac{|e|\hbar B}{mc} + \frac{p_z^2}{2m} - (\mu/s)\,\sigma B, \tag{4.4}$$

where n is any integer [107]. These quantum numbers n specify states known as Landau levels. For the case in which the motion of particles in restricted to a rectangular geometry of $L_x \times L_y$, also let $p_z = 0$ as the motion of particles is restricted in this case to only the $x - y$ plane. In this case the energy of each Landau level is given by

$$E = \left(n + \frac{1}{2}\right)\frac{|e|\hbar B}{mc} - (\mu/s)\,\sigma B. \tag{4.5}$$

Due to the restriction that $\hbar\omega \gg k_BT$, thermal excitations can be neglected because the interval between Landau levels is much greater than thermal excitation energy. As a result, the probability that electrons will be thermally excited to higher energy levels can be neglected. In order to fill higher energy levels the density of states must be increased. When the Landau level is fully occupied from the lowest to the ith energy level the transverse resistivity becomes

$$\rho_{xy} = \frac{h}{ie^2}, \tag{4.6}$$

where i is any integer corresponding to a specific filled Landau level, e is the charge of an electron, and h is Planck's constant [104, 105]. Eq. 4.6 shows that at critical values of the field, the Hall resistivity (or conductivity) is quantized in units of h/e^2 [78, 106]. Fig. 4.1 demonstrates an example of the quantized

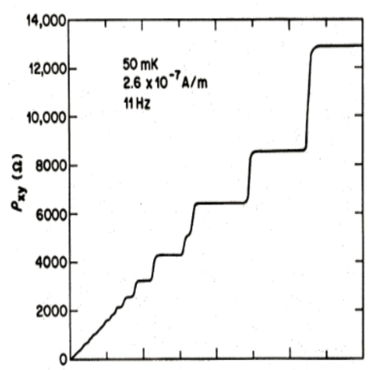

Figure 4.1: ρ_{xy} as a function of magnetic field B at low temperature ($T = 50\,\mathrm{mK}$). Figure originally appeared in ref. [110].

nature of the transverse resistivity. The distance between each plateau (step height) is given by h/e^2 divided by an integer i. These steplike increases with plateaus in the magnetic field region where the longitudinal resistivity ρ_{xx} vanished [111]. Thus, when $\rho_{xx} = 0$ then $\rho_{xy} = h/ie^2$ and is at a plateau. Note that the temperatures needed to observe the IQHE ($\lesssim 4\,\mathrm{K}$) is a likely reason why it was not discovered until 1980. It is also important to note that the value of resistivity only depends on fundamental constants of physics and can be used as a primary resistance standard known as the von Klitzing constant, $R_{\mathrm{K}-90} = 25812.807\,\Omega$ [104, 112, 113]. Observation of the IQHE confirms the high-quality nature of the device in question as it is necessary to obtain high mobilities at very low temperatures. Furthermore, this would offer a more complete picture of the quantum structure of under the high-field limit and allow for the measurement of further quantum properties that reveal important information about the underlying structure of the device.

4.2 Shubnikov-de Haas Oscillations

There are several techniques and measurements that can determine the geometry of the Fermi surface, many of these are closely related to one another and are based on the same underlying mechanism. One such effect is the SdH effect [114]. The SdH effect is an oscillatory dependence of the resistivity on the magnetic field, there it is related to the quantum hall effect (QHE) [115]. This effect is produced by the oscillation of the density of states at the Fermi level which is caused by the quantization of electron energy levels in the presence of a magnetic field (see sec. 4.1, Landau levels) [116, 117]. The oscillations occur with a periodicity of B^{-1} [118].

SdH oscillations can provide a wealth of information about the effective 2DEG (2DHG). For exam-

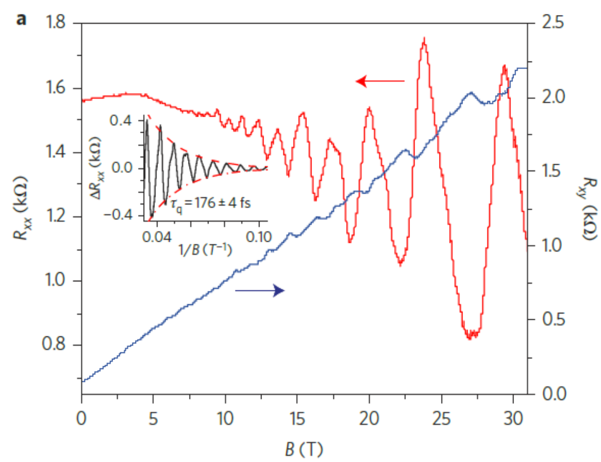

Figure 4.2: Longitudinal resistance R_{xx} (red curve) and Hall resistance R_{xy} (blue curve) of an encapsulated hBN CVD monolayer MoS_2 device as a function of magnetic field B at $T = 0.3\,\mathrm{K}$ with carrier density $n = 9.7 \times 10^{12}\,\mathrm{cm}^{-2}$. Inset: Oscillation amplitude (black curve) as a function of B^{-1} with fitted plot for obtaining τ_q. Figure appeared in ref [119].

ple, one can extract the carrier lifetimes, effective cyclotron mass, information about the Fermi surface [75]. In order to observe the QHE and therefore observe SdH oscillations, high device mobility is required [120, 121]. Recently the Cui *et al.* observed the first SdH oscillations in MoS_2, Li *et al.* and Gillgren *et al.* observed this same effect in black phosphorus (and phosphorene) [119, 75, 122]. Cui *et al.* were able to determine geometry of the Fermi surface from the oscillation frequency and prove the two-dimensional nature of their system. Furthermore, from the analysis of the oscillation amplitude the cyclotron effective masses of both electrons and holes could be determined. From this method the carrier lifetime could also be determined, they reported lifetimes of $\tau = 0.11\,\mathrm{ps}$ and $\tau = 0.12\,\mathrm{ps}$ for holes and electrons, respectively [75, 118]. Cui *et al.* was able to provide insight about the quantum lifetimes and the underlying interactions between short-range and long-range scattering limits [119]. Fig. 4.2 shows the results from Cui *et al.*. The red curve shows the longitudinal resistance R_{xx}, the blue curve shows the Hall resistance R_{xy} both as a function of magnetic field B. The curve for R_{xy} shows the plateaus for corresponding to the Landau levels. The inset of the curve also shows the SdH oscillations as a function of B^{-1}, from this curve the quantum scattering lifetime of $\tau_q = 0.18\,\mathrm{ps}$ in CVD monolayer MoS_2 is found by using a fit. The results provide promise that with the implementations of improvements in contact resistance reduction and further mobility enhancement that the world of TMDs is closer to the routine study of novel quantum physics in two-dimensional systems.

4.3 Performance Limits in TMDs

The ultimate performance limit of TMDs is of interest, especially at room temperature as this is most relevant to device applications. First principles calculations show mobility in monolayer MoS_2 to be $\sim 320 - 410\,\mathrm{cm^2V^{-1}s^{-1}}$ at room temperature depending on initial parameters [123, 124]. Previously the experimental values reported differed by an order of magnitude compared to first principles calculations, however, the improvements made in the area of reducing contact resistance has improved mobility measurements [125, 126]. Experimentally, room temperature mobility measurements of both p and n type semiconductors still lag behind the theoretical calculations. For example, WSe_2 room temperature mobilities have been reported as $\sim 200\,\mathrm{cm^2V^{-1}s^{-1}}$ with perfect subthreshold swings of $\sim 60\,\mathrm{mV/\,dec}$, a $I_{\mathrm{on}}/I_{\mathrm{off}}$ of $> 10^6$ at room temperature (others have shown $I_{\mathrm{on}}/I_{\mathrm{off}}$ of $> 10^7$ in WSe_2 and MoS_2), and high $I_{\mathrm{on}} \sim 300\,\mu\mathrm{A}/\,\mu\mathrm{m}$ [59, 127, 67, 88]. Undoped samples have shown to have room temperature mobility of an order of magnitude less than the doped counterparts [128, 88]. Note that these values are not the theoretical limits, but rather represent a current state of where measurements can achieve. To further improve the mobilities measured at room temperature a further understanding of scattering mechanisms is needed. At room temperature phonon scattering limits the mobility, the mobility can be enhanced by doping, however, this introduces impurities and can have an adverse effect on the mobility. Understanding the performance limit at room temperature in monolayers (and few layers) is key to applications in which several TMDs are already being implemented, such as thin film transistor (TFT) and components of ICs like analog amplifiers, digital inverters, and memory transistors [129, 24, 130].

4.4 Conclusion

Overall, TMDs offer a wealth of opportunities in applications. In order to realize these proposed applications several challenges must be overcome, namely achieving low-resistance contacts and high mobility at room temperature. The approach of using degenerately doped contacts and hBN encapsulated devices to lower the SBH and promote increased mobility has shown potential. In addition, the increased mobility that the success of this method would allow one to study quantum transport properties which will reveal many fundamental properties, such as quantum scattering times and effective masses.

References

[1] J Koenigsberger and J Weiss. Über die thermoelektrischen effekte (thermokräfte, thomsonwärme) und die wärmeleitung in einigen elementen und verbindungen und über die experimentelle prüfung der elektronentheorien. *Annalen der Physik*, 340(6):1–46, 1911.

[2] G. Busch. Early history of the physics and chemistry of semiconductors-from doubts to fact in a hundred years. *European Journal of Physics*, 10:254–264, oct 1989.

[3] KARL Lark-Horovitz. The present state of physics. *Am. Assoc. Advancement Sci., Washington, DC*, page 57, 1954.

[4] A. H. Wilson. The theory of electronic semi-conductors. *Proceedings of the Royal Society of London. Series A, Containing Papers of a Mathematical and Physical Character*, 133(822):458–491, 1931.

[5] A. H. Wilson. The theory of electronic semi-conductors. ii. *Proceedings of the Royal Society of London. Series A, Containing Papers of a Mathematical and Physical Character*, 134(823):277–287, 1931.

[6] Donald A. Neaman. *Semiconductor Physics and Devices: Basic Principles*. McGraw-Hill, New York, NY, 3 edition, 2003.

[7] Lidia Łukasiak and Andrzej Jakubowski. History of semiconductors. *Journal of Telecommunications and information technology*, pages 3–9, 2010.

[8] Jack S. Kilby. Miniaturized electronic circuits. United States Patent Office, 1959. U.S. Patent 3,138,743, issued June 1964.

[9] G. Moore. Cramming more components onto integrated circuits. *Electronics*, 38(8), 1965.

[10] Peter Clarke. Intel enters billion-transistor processor era, October 2005. [Online; 13 accessed-December-2015].

[11] James D. Meindl, Qiang Chen, and Jeffrey A. Davis. Limits on silicon nanoelectronics for terascale integration. *Science*, 293(5537):2044–2049, 2001.

[12] Max Schulz. The end of the road for silicon? *Nature*, 399:729–730, 1999.

[13] Joshua Golden, Melissa McMillan, Robert T Downs, Grethe Hystad, Ian Goldstein, Holly J Stein, Aaron Zimmerman, Dimitri A Sverjensky, John T Armstrong, and Robert M Hazen. Rhenium variations in molybdenite (mos 2): Evidence for progressive subsurface oxidation. *Earth and Planetary Science Letters*, 366:1–5, 2013.

[14] Benjamin C Brodie. On the atomic weight of graphite. *Philosophical Transactions of the Royal Society of London*, pages 249–259, 1859.

[15] H. W. Kroto, J. R. Heath, S. C. O'Brien, R. F. Curl, and R. E. Smalley. C60: Buckminsterfullerene. *Nature*, 318:162–163, 1985.

[16] Ruben Mas-Balleste, Cristina Gomez-Navarro, Julio Gomez-Herrero, and Felix Zamora. 2d materials: to graphene and beyond. *Nanoscale*, 3:20–30, 2011.

[17] Sumio Iijima. Helical microtubules of graphitic carbon. *Nature*, 354:56–58, 1991.

[18] K. S. Novoselov, A. K. Geim, S. V. Morozov, D. Jiang, Y. Zhang, S. V. Dubonos, I. V. Grigorieva, and A. A. Firsov. Electric field effect in atomically thin carbon films. *Science*, 306(5696):666–669, 2004.

[19] A. K. Geim and K. S. Novoselov. The rise of graphene. *Nature Materials*, 6:183–191, 2007.

[20] K.S. Novoselov, A. K. Geim, S.V. Morozov, D. Jiang, M.I. Katsnelson, I.V. Grigorieva, S.V. Dubonos, and A.A. Firsov. Two-dimensional gas of massless dirac fermions in graphene. *Nature*, 438:197–200, 2005.

[21] L. Zhang, Y. Zhang, J. Camacho, M. Khodas, and I. Zaliznyak. The experimental observation of quantum hall effect of l=3 chiral quasiparticles in trilayer graphene. *Nat. Phys.*, 7:953–957, 2011.

[22] J. R. Williams, L. DiCarlo, and C. M. Marcus. Quantum hall effect in a gate-controlled p-n junction of graphene. *Science*, 317(5838):638–641, 2007.

[23] Simone Bertolazzi, Jacopo Brivio, and Andras Kis. Stretching and breaking of ultrathin mos2. *ACS Nano*, 5(12):9703–9709, 2011. PMID: 22087740.

[24] Deji Akinwande, Nicholas Petron, and James Hone. Two-dimensional flexible nanoelectronics. *Nature Communications*, 5, 2014.

[25] A. Dargys and J. Kundrotas. *Handbook on physical properties of Ge, Si, GaAs, InP.* Science and Encyclopedia Publishers, Vilnius, Lithuania, 1994.

[26] Ioffe Institute Database. Electrical properties of silicon. http://www.ioffe.rssi.ru/SVA/NSM/Semicond/Si/electric.htm [Online; Accessed 1 Feb. 2016].

[27] K.S. Novoselov and A.K. Geim. The rise of graphene. *Nature Materials*, 6:183–191, 2007.

[28] Berkley Labs. Bilayer graphene gets a bandgap, June 2009. [Online; 23 accessed-December-2015].

[29] P. R. Wallace. The band theory of graphite. *Phys. Rev.*, 71:622–634, May 1947.

[30] Mingsheng Xu, Tao Liang, Minmin Shi, and Hongzheng Chen. Graphene-like two-dimensional materials. *Chemical Reviews*, 113(5):3766–3798, 2013. PMID: 23286380.

[31] F.N. Xia, T. Mueller, Y.M. Lin, A. Valdes-Garcia, and P. Avouris. Ultrafast graphene photodetector. *Nat. Nanotechnol.*, 4:839–843, 2009.

[32] Feng Wang, Yuanbo Zhang, Chuanshan Tian, Caglar Girit, Alex Zettl, Michael Crommie, and Y. Ron Shen. Gate-variable optical transitions in graphene. *Science*, 320(5873):206–209, 2008.

[33] T.J. Echtermeyer, L. Britnell, P.K. Jasnos, A. Lombardo, R.V. Gorbachev, A.N. Grigorenko, A.K. Geim, A.C. Ferrari, and K.S. Novoselov. Strong plasmonic enhancement of photovoltage in graphene. *Nat. Commun.*, 2:458, 2011.

[34] Kyozaburo Takeda and Kenji Shiraishi. Theoretical possibility of stage corrugation in si and ge analogs of graphite. *Phys. Rev. B*, 50:14916–14922, Nov 1994.

[35] S. Cahangirov, M. Topsakal, E. Aktürk, H. Şahin, and S. Ciraci. Two- and one-dimensional honeycomb structures of silicon and germanium. *Phys. Rev. Lett.*, 102:236804, Jun 2009.

[36] R. F. Frindt and A. D. Yoffe. Physical properties of layer structures: Optical properties and photoconductivity of thin crystals of molybdenum disulphide. *Proceedings of the Royal Society of London A: Mathematical, Physical and Engineering Sciences*, 273(1352):69–83, 1963.

[37] R. Fivaz and E. Mooser. Mobility of charge carriers in semiconducting layer structures. *Phys. Rev.*, 163:743–755, Nov 1967.

[38] L. F. Mattheiss. Band structures of transition-metal-dichalcogenide layer compounds. *Phys. Rev. B*, 8:3719–3740, Oct 1973.

[39] J.A. Wilson and A.D. Yoffe. The transition metal dichalcogenides discussion and interpretation of the observed optical, electrical and structural properties. *Advances in Physics*, 18(73):193–335, 1969.

[40] AF Wells. Structural inorganic chemistryoxford univ. press, 1984.

[41] B. Radisavljevic, A. Radenovic, J. Brivio, V. Giacometti, and A. Kis. Single-layer mos2 transistors. *Nat. Nano.*, 6:147–150, 2011.

[42] Murong Lang, Liang He, Faxian Xiu, Xinxin Yu, Jianshi Tang, Yong Wang, Xufeng Kou, Wanjun Jiang, Alexei V. Fedorov, and Kang L. Wang. Revelation of topological surface states in bi2se3 thin films by in situ al passivation. *ACS Nano*, 6(1):295–302, 2012. PMID: 22147687.

[43] Hong Bin Zhang, Hai Lin Yu, Ding Hua Bao, Shu Wei Li, Cheng Xin Wang, and Guo Wei Yang. Magnetoresistance switch effect of a sn-doped bi2te3 topological insulator. *Advanced Materials*, 24(1):132–136, 2012.

[44] Wenjie Xie, Xinfeng Tang, Yonggao Yan, Qingjie Zhang, and Terry M. Tritt. Unique nanostructures and enhanced thermoelectric performance of melt-spun bisbte alloys. *Applied Physics Letters*, 94(10):–, 2009.

[45] F. R. Gamble and B. G. Silbernagel. Anisotropy of the proton spinlattice relaxation time in the superconducting intercalation complex tas2(nh3): Structural and bonding implications. *The Journal of Chemical Physics*, 63(6):2544–2552, 1975.

[46] Yoichi Kubota, Kenji Watanabe, Osamu Tsuda, and Takashi Taniguchi. Deep ultraviolet light-emitting hexagonal boron nitride synthesized at atmospheric pressure. *Science*, 317(5840):932–934, 2007.

[47] Ki Kang Kim, Allen Hsu, Xiaoting Jia, Soo Min Kim, Yumeng Shi, Mario Hofmann, Daniel Nezich, Joaquin F Rodriguez-Nieva, Mildred Dresselhaus, Tomas Palacios, et al. Synthesis of monolayer hexagonal boron nitride on cu foil using chemical vapor deposition. *Nano letters*, 12(1):161–166, 2011.

[48] Li Song, Lijie Ci, Hao Lu, Pavel B Sorokin, Chuanhong Jin, Jie Ni, Alexander G Kvashnin, Dmitry G Kvashnin, Jun Lou, Boris I Yakobson, et al. Large scale growth and characterization of atomic hexagonal boron nitride layers. *Nano letters*, 10(8):3209–3215, 2010.

[49] Kin Fai Mak, Changgu Lee, James Hone, Jie Shan, and Tony F Heinz. Atomically thin mos 2: a new direct-gap semiconductor. *Physical Review Letters*, 105(13):136805, 2010.

[50] E Gourmelon, O Lignier, H Hadouda, G Couturier, JC Bernede, J Tedd, J Pouzet, and J Salardenne. Ms 2 (m= w, mo) photosensitive thin films for solar cells. *Solar energy materials and solar cells*, 46(2):115–121, 1997.

[51] E Fortin and WM Sears. Photovoltaic effect and optical absorption in mos 2. *Journal of Physics and Chemistry of Solids*, 43(9):881–884, 1982.

[52] Agnieszka Kuc, Nourdine Zibouche, and Thomas Heine. Influence of quantum confinement on the electronic structure of the transition metal sulfide t s 2. *Physical Review B*, 83(24):245213, 2011.

[53] Yandong Ma, Ying Dai, Meng Guo, Chengwang Niu, Jibao Lu, and Baibiao Huang. Electronic and magnetic properties of perfect, vacancy-doped, and nonmetal adsorbed mose 2, mote 2 and ws 2 monolayers. *Physical Chemistry Chemical Physics*, 13(34):15546–15553, 2011.

[54] Qing Hua Wang, Kourosh Kalantar-Zadeh, Andras Kis, Jonathan N Coleman, and Michael S Strano. Electronics and optoelectronics of two-dimensional transition metal dichalcogenides. *Nature nanotechnology*, 7(11):699–712, 2012.

[55] Rui Cheng, Dehui Li, Hailong Zhou, Chen Wang, Anxiang Yin, Shan Jiang, Yuan Liu, Yu Chen, Yu Huang, and Xiangfeng Duan. Electroluminescence and photocurrent generation from atomically sharp wse2/mos2 heterojunction p–n diodes. *Nano letters*, 14(10):5590–5597, 2014.

[56] Hiram J Conley, Bin Wang, Jed I Ziegler, Richard F Haglund Jr, Sokrates T Pantelides, and Kirill I Bolotin. Bandgap engineering of strained monolayer and bilayer mos2. *Nano letters*, 13(8):3626–3630, 2013.

[57] Seunghyun Lee and Zhaohui Zhong. Nanoelectronic circuits based on two-dimensional atomic layer crystals. *Nanoscale*, 6(22):13283–13300, 2014.

[58] Andrea Splendiani, Liang Sun, Yuanbo Zhang, Tianshu Li, Jonghwan Kim, Chi-Yung Chim, Giulia Galli, and Feng Wang. Emerging photoluminescence in monolayer mos2. *Nano letters*, 10(4):1271–1275, 2010.

[59] Hui Fang, Steven Chuang, Ting Chia Chang, Kuniharu Takei, Toshitake Takahashi, and Ali Javey. High-performance single layered wse2 p-fets with chemically doped contacts. *Nano letters*, 12(7):3788–3792, 2012.

[60] Saptarshi Das and Joerg Appenzeller. Wse2 field effect transistors with enhanced ambipolar characteristics. *Applied Physics Letters*, 103(10):103501, 2013.

[61] Han Liu, Adam T Neal, and Peide D Ye. Channel length scaling of mos2 mosfets. *ACS nano*, 6(10):8563–8569, 2012.

[62] Saptarshi Das, Hong-Yan Chen, Ashish Verma Penumatcha, and Joerg Appenzeller. High performance multilayer mos2 transistors with scandium contacts. *Nano letters*, 13(1):100–105, 2012.

[63] Cheng Gong, Luigi Colombo, Robert M Wallace, and Kyeongjae Cho. The unusual mechanism of partial fermi level pinning at metal–mos2 interfaces. *Nano letters*, 14(4):1714–1720, 2014.

[64] Joonki Suh, Tae-Eon Park, Der-Yuh Lin, Deyi Fu, Joonsuk Park, Hee Joon Jung, Yabin Chen, Changhyun Ko, Chaun Jang, Yinghui Sun, et al. Doping against the native propensity of mos2: Degenerate hole doping by cation substitution. *Nano letters*, 14(12):6976–6982, 2014.

[65] Andre K Geim and Irina V Grigorieva. Van der waals heterostructures. *Nature*, 499(7459):419–425, 2013.

[66] Mojtaba Farmanbar and Geert Brocks. Controlling the schottky barrier at mos 2/metal contacts by inserting a bn monolayer. *Physical Review B*, 91(16):161304, 2015.

[67] Rajesh Kappera, Damien Voiry, Sibel Ebru Yalcin, Brittany Branch, Gautam Gupta, Aditya D Mohite, and Manish Chhowalla. Phase-engineered low-resistance contacts for ultrathin mos2 transistors. *Nature materials*, 13(12):1128–1134, 2014.

[68] Mojtaba Farmanbar and Geert Brocks. Ohmic contacts to 2d semiconductors through van der waals bonding. *arXiv preprint arXiv:1601.02163*, 2016.

[69] Robert W Keyes. The electrical properties of black phosphorus. *Physical Review*, 92(3):580, 1953.

[70] Y Maruyama, S Suzuki, K Kobayashi, and S Tanuma. Synthesis and some properties of black phosphorus single crystals. *Physica B+ C*, 105(1):99–102, 1981.

[71] Vy Tran, Ryan Soklaski, Yufeng Liang, and Li Yang. Layer-controlled band gap and anisotropic excitons in few-layer black phosphorus. *Phys. Rev. B*, 89:235319, Jun 2014.

[72] Likai Li, Yijun Yu, Guo Jun Ye, Qingqin Ge, Xuedong Ou, Hua Wu, Donglai Feng, Xian Hui Chen, and Yuanbo Zhang. Black phosphorus field-effect transistors. *Nature nanotechnology*, 9(5):372–377, 2014.

[73] Steven P Koenig, Rostislav A Doganov, Hennrik Schmidt, AH Castro Neto, and Barbaros Oezyilmaz. Electric field effect in ultrathin black phosphorus. *Applied Physics Letters*, 104(10):103106, 2014.

[74] Fengnian Xia, Han Wang, and Yichen Jia. Rediscovering black phosphorus as an anisotropic layered material for optoelectronics and electronics. *Nature communications*, 5, 2014.

[75] Likai Li, Guo Jun Ye, Vy Tran, Ruixiang Fei, Guorui Chen, Huichao Wang, Jian Wang, Kenji Watanabe, Takashi Taniguchi, Li Yang, et al. Quantum oscillations in a two-dimensional electron gas in black phosphorus thin films. *Nature nanotechnology*, 2015.

[76] Rino Choi, Chang Seok Kang, Hag-Ju Cho, Young-Hee Kim, Mohammad S. Akbar, and Jack C. Lee. Effects of high temperature forming gas anneal on the characteristics of metal-oxide-semiconductor field-effect transistor with hfo2 gate stack. *Applied Physics Letters*, 84(24):4839–4841, 2004.

[77] Yuan Huang, Eli Sutter, Norman N. Shi, Jiabao Zheng, Tianzhong Yang, Dirk Englund, Hong-Jun Gao, and Peter Sutter. Reliable Exfoliation of Large-Area High-Quality Flakes of Graphene and Other Two-Dimensional Materials. *ACS Nano*, 0(0):null, 0. PMID: 26336975.

[78] C. Kittel. *Introduction to Solid State Physics*. Wiley, Hoboken, N. J., 8 edition, 2005.

[79] Ernst Moritz Arndt Universität Greifswald: Soft Matter and Biophysics. AFM (Atomic Force Microscope, 2015. [Online; Accessed: 22, Jan. 2016].

[80] Joe Nabity. NPGS: Nanometer Pattern Generation System, January 2016. [Online; Accessed: 26, Jan. 2016].

[81] W Schottky. Semiconductor theory of the blocking layer. *Naturwissenschaften*, 26:843, 1938. in German.

[82] VL Rideout. A review of the theory and technology for ohmic contacts to group iii–v compound semiconductors. *Solid-State Electronics*, 18(6):541–550, 1975.

[83] Emlyn Huw Rhoderick and Richard H Williams. *Metal-semiconductor contacts*, volume 129. Clarendon Press Oxford, 1988.

[84] Simon S Cohen and Gennady Sh Gildenblat. *Metal–Semiconductor Contacts and Devices: VLSI Electronics Microstructure Science*, volume 13. Academic Press, 2014.

[85] Raymond T. Tung. The physics and chemistry of the schottky barrier height. *Applied Physics Reviews*, 1(1), 2014.

[86] Yuanyue Liu, Paul Stradins, and Su-Huai Wei. Van der waals metal-semiconductor junction: weak fermi level pinning enables effective tuning of schottky barrier. *arXiv preprint arXiv:1601.03845*, 2016.

[87] Hsun-Jen Chuang, Xuebin Tan, Nirmal Jeevi Ghimire, Meeghage Madusanka Perera, Bhim Chamlagain, Mark Ming-Cheng Cheng, Jiaqiang Yan, David Mandrus, David Tomnek, and Zhixian Zhou. High mobility wse2 p- and n-type field-effect transistors contacted by highly doped graphene for low-resistance contacts. *Nano Letters*, 14(6):3594–3601, 2014. PMID: 24844426.

[88] Saptarshi Das, Richard Gulotty, Anirudha V Sumant, and Andreas Roelofs. All two-dimensional, flexible, transparent, and thinnest thin film transistor. *Nano letters*, 14(5):2861–2866, 2014.

[89] Tania Roy, Mahmut Tosun, Jeong Seuk Kang, Angada B. Sachid, Sujay B. Desai, Mark Hettick, Chenming C. Hu, and Ali Javey. Field-effect transistors built from all two-dimensional material components. *ACS Nano*, 8(6):6259–6264, 2014. PMID: 24779528.

[90] Yuan Liu, Hao Wu, Hung-Chieh Cheng, Sen Yang, Enbo Zhu, Qiyuan He, Mengning Ding, Dehui Li, Jian Guo, Nathan O Weiss, et al. Toward barrier free contact to molybdenum disulfide using graphene electrodes. *Nano letters*, 15(5):3030–3034, 2015.

[91] Hsun-Jen Chuang, Bhim Prasad Chamlagain, Michael Koehler, Meeghage Madusanka Perera, Jiaqiang Yan, David Mandrus, David Tomanek, and Zhixian Zhou. Low-resistance 2d/2d ohmic contacts: A universal approach to high-performance wse2, mos2, and mose2 transistors. *Nano Letters*, 0(ja):null, 0.

[92] Dieter K. Schroder. *Semiconductor Material and Device Characterization*. John Wiley and Sons, Inc., Hoboken, New Jersey, 3rd edition, 2006.

[93] Lingming Yang, Kausik Majumdar, Han Liu, Yuchen Du, Heng Wu, Michael Hatzistergos, PY Hung, Robert Tieckelmann, Wilman Tsai, Chris Hobbs, et al. Chloride molecular doping technique on 2d materials: Ws2 and mos2. *Nano letters*, 14(11):6275–6280, 2014.

[94] Wei Sun Leong, Xin Luo, Yida Li, Khoong Hong Khoo, Su Ying Quek, and John TL Thong. Low resistance metal contacts to mos2 devices with nickel-etched-graphene electrodes. *ACS nano*, 9(1):869–877, 2014.

[95] A. F. Stassen, R. W. I. de Boer, N. N. Iosad, and A. F. Morpurgo. Influence of the gate dielectric on the mobility of rubrene single-crystal field-effect transistors. *Applied Physics Letters*, 85:3899, oct 2004.

[96] Leopoldo B Valdes. Resistivity measurements on germanium for transistors. *Proceedings of the IRE*, 42(2):420–427, 1954.

[97] Britton W. H. Baugher, Hugh O. H. Churchill, Yafang Yang, and Pablo Jarillo-Herrero. Intrinsic electronic transport properties of high-quality monolayer and bilayer mos2. *Nano Letters*, 13(9):4212–4216, 2013. PMID: 23930826.

[98] NR Pradhan, D Rhodes, S Memaran, JM Poumirol, D Smirnov, S Talapatra, S Feng, N Perea-Lopez, AL Elias, M Terrones, et al. Hall and field-effect mobilities in few layered p-wse2 field-effect transistors. *Scientific reports*, 5, 2015.

[99] Tsuneya Ando, Alan B Fowler, and Frank Stern. Electronic properties of two-dimensional systems. *Reviews of Modern Physics*, 54(2):437, 1982.

[100] Adrian Constantin Melissinos and Adrian C Melissinos. *Experiments in modern physics*, volume 114. Academic Press Orlando), 1966.

[101] Thurber W.R. NIST: Hall effect measurements, Nov. 2011. [Online; Accessed: 26, Jan. 2016].

[102] Nobelprize.org. Press release: The 1998 nobel prize in physics, 2016. [Online; Accessed: 26, Jan. 2016].

[103] Neil W Ashcroft, N David Mermin, and Sergio Rodriguez. Solidstatephysics. *American Journal of Physics*, 46(1):116–117, 1978.

[104] K. v. Klitzing, G. Dorda, and M. Pepper. New method for high-accuracy determination of the fine-structure constant based on quantized hall resistance. *Phys. Rev. Lett.*, 45:494–497, Aug 1980.

[105] M. O. Goerbig. Quantum Hall Effects. *ArXiv e-prints*, sep 2009. Provided by the SAO/NASA Astrophysics Data System.

[106] J.R. Hook and E. Hall, H. *Solid State Physics*. Wiley, West Sussex, England, 2 edition, 1991.

[107] Lev Davidovich Landau and Evgenii Mikhailovich Lifshitz. *Quantum mechanics: non-relativistic theory*, volume 3. Addison-Wesley, Reading, MA., 1965.

[108] Jun John Sakurai and Jim J Napolitano. *Modern quantum mechanics*. Addison-Wesley, Reading, MA., 1994.

[109] LD Landau. Diamagnetismus der metalle. *Zeitschrift für Physik*, 64(9-10):629–637, 1930.

[110] M. A. Paalanen, D. C. Tsui, and A. C. Gossard. Quantized hall effect at low temperatures. *Phys. Rev. B*, 25:5566–5569, Apr 1982.

[111] Klaus von Klitzing. The quantized hall effect. *Rev. Mod. Phys.*, 58:519–531, Jul 1986.

[112] Hideo Aoki and Tsuneya Ando. Universality of quantum hall effect: Topological invariant and observable. *Phys. Rev. Lett.*, 57:3093–3096, Dec 1986.

[113] L Bliek. Present understanding of the quantum hall effect. *Metrologia*, 25(2):67, 1988.

[114] LV Shubnikov and WJ de Haas. Leiden commun. 207a (1930). *Proc. Netherlands R. Acad. Sci*, 33:130–163, 1930.

[115] D. E. Soule, J. W. McClure, and L. B. Smith. Study of the shubnikov-de haas effect. determination of the fermi surfaces in graphite. *Phys. Rev.*, 134:A453–A470, Apr 1964.

[116] R Peierls. On the theory of the diamagnetism of conduction electrons. ii strong magnetic fields. *Z. Phys*, 81:186–194, 1933.

[117] LD Landau. See appendix to d. shoenberg. In *Proc. Roy. Soc. A*, volume 170, page 341, 1939.

[118] David Shoenberg. *Magnetic oscillations in metals*. Cambridge University Press, 1984.

[119] Xu Cui, Gwan-Hyoung Lee, Young Duck Kim, Ghidewon Arefe, Pinshane Y Huang, Chul-Ho Lee, Daniel A Chenet, Xian Zhang, Lei Wang, Fan Ye, et al. Multi-terminal transport measurements of mos2 using a van der waals heterostructure device platform. *Nature nanotechnology*, 2015.

[120] Sankar Das Sarma and Aron Pinczuk. Perspectives in quantum hall effects: Novel quantum liquids in low-dimensional semiconductor structures. *Perspectives in Quantum Hall Effects: Novel Quantum Liquids in Low-Dimensional Semiconductor Structures, by Sankar Das Sarma (Editor), Aron Pinczuk (Editor), pp. 446. ISBN 0-471-11216-X. Wiley-VCH, November 1996.*, 1, 1996.

[121] A. Tsukazaki, A. Ohtomo, T. Kita, Y. Ohno, H. Ohno, and M. Kawasaki. Quantum Hall Effect in Polar Oxide Heterostructures. *Science*, 315:1388–, mar 2007.

[122] Nathaniel Gillgren, Darshana Wickramaratne, Yanmeng Shi, Tim Espiritu, Jiawei Yang, Jin Hu, Jiang Wei, Xue Liu, Zhiqiang Mao, Kenji Watanabe, Takashi Taniguchi, Marc Bockrath, Yafis Barlas, Roger K Lake, and Chun Ning Lau. Gate tunable quantum oscillations in air-stable and high mobility few-layer phosphorene heterostructures. *2D Materials*, 2(1):011001, 2015.

[123] Xiaodong Li, Jeffrey T Mullen, Zhenghe Jin, Kostyantyn M Borysenko, M Buongiorno Nardelli, and Ki Wook Kim. Intrinsic electrical transport properties of monolayer silicene and mos 2 from first principles. *Physical Review B*, 87(11):115418, 2013.

[124] Kristen Kaasbjerg, Kristian S Thygesen, and Karsten W Jacobsen. Phonon-limited mobility in n-type single-layer mos 2 from first principles. *Physical Review B*, 85(11):115317, 2012.

[125] Branimir Radisavljevic, Aleksandra Radenovic, Jacopo Brivio, V Giacometti, and A Kis. Single-layer mos2 transistors. *Nature nanotechnology*, 6(3):147–150, 2011.

[126] Rajesh Kappera, Damien Voiry, Sibel Ebru Yalcin, Wesley Jen, Muharrem Acerce, Sol Torrel, Brittany Branch, Sidong Lei, Weibing Chen, Sina Najmaei, et al. Metallic 1t phase source/drain electrodes for field effect transistors from chemical vapor deposited mos2. *APL Materials*, 2(9):092516, 2014.

[127] Wei Liu, Jiahao Kang, Deblina Sarkar, Yasin Khatami, Debdeep Jena, and Kaustav Banerjee. Role of metal contacts in designing high-performance monolayer n-type wse2 field effect transistors. *Nano letters*, 13(5):1983–1990, 2013.

[128] Song-Lin Li, Katsunori Wakabayashi, Yong Xu, Shu Nakaharai, Katsuyoshi Komatsu, Wen-Wu Li, Yen-Fu Lin, Alex Aparecido-Ferreira, and Kazuhito Tsukagoshi. Thickness-dependent interfacial coulomb scattering in atomically thin field-effect transistors. *Nano letters*, 13(8):3546–3552, 2013.

[129] Ganesh R Bhimanapati, Zhong Lin, Vincent Meunier, Yeonwoong Jung, Judy Cha, Saptarshi Das, Di Xiao, Youngwoo Son, Michael S Strano, Valentino R Cooper, et al. Recent advances in two-dimensional materials beyond graphene. *ACS nano*, 9(12):11509–11539, 2015.

[130] Hee Sung Lee, Sung-Wook Min, Min Kyu Park, Young Tack Lee, Pyo Jin Jeon, Jae Hoon Kim, Sunmin Ryu, and Seongil Im. Mos2 nanosheets for top-gate nonvolatile memory transistor channel. *Small*, 8(20):3111–3115, 2012.

Appendices

2DEG two-dimensional electron gas

2DES two-dimensional electron system

2DHG two-dimensional hole gas

AFM atomic force microscopy

Au gold

BJD Bell Jar deposition

BP black phosphorus

CBM conduction band minimum

CVD chemical vapor deposition

DI deionized water

DFT density functional theory

EBL electron beam lithography

FET field effect transistor

IC integrated circuit

IPA isopropanol

IQHE integer quantum Hall effect

MEK methyl ethyl ketone

MFM magnetic force microscopy

MIBK methyl isobutyl ketone

Mo molybdenum

MoS_2 molybdenum disulfide

N_2 nitrogen

Nb niobium

Ni nickel

NPGS Nanometer Pattern Generation System

PC polycarbonate

PDMS polydimethylsiloxane

PMMA polymethyl methacrylate

PPMS physical property measurement system

QHE quantum hall effect

Re rhenium

S sulfur

SB Schottky barrier

SBH Schottky barrier height

Se selenium

SEM scanning electron microscope

SdH Shubnikov-de Haas

SiO_2 silicon dioxide

STM scanning tunneling microscopy

Te tellurium

TEM transmission electron microscopy

TFT thin film transistor

Ti titanium

TLM transmission line model

TMD transition metal dichalcogenides

V vanadium

VBM valence band maximum

W tungsten

WS_2 tungsten disulfide

WSe_2 tungsten diselenide

ACKNOWLEDGEMENTS

I would like to acknowledge the continued guidance, help, and support from my advisor Dr. Zhixian Zhou. I am also grateful to Hsun Jen (Ben) Chuang, Bhim Chamlagain, Meeghage Madusanka Perera, Arthur Bowman III, Upendra Rijal, and Sagar Paudel for their advice and cooperation. Finally, I would like to thank the committee members Dr. Jian Huang, Dr. Mark Ming-Cheng Cheng and Dr. Ashis Mukhopadhyay for their valuable time.